Understanding the (de)sodiation mechanisms in Na-based batteries through Operando X-ray methods

Anders Brennhagen, Carmen Cavallo, David D. Wragg, Jonas Sottmann, Alexey Y. Koposov, Helmer Fjellvag

Batteries & Supercaps

Chemistry Europe
European Chemical Societies Publishing

Accepted Article

Title: Understanding the (de)sodiation mechanisms in Na-based batteries through Operando X-ray methods

Authors: Anders Brennhagen, Carmen Cavallo, David Wragg, Jonas Sottmann, Alexey Y. Koposov, and Helmer Fjellvåg

To be cited as: *Batteries & Supercaps* 10.1002/batt.202000294

Link to VoR: https://doi.org/10.1002/batt.202000294

WILEY-VCH

10.1002/batt.202000294

Understanding the (de)sodiation mechanisms in Na-based batteries through *Operando* X-ray methods

Anders Brennhagen[1], Carmen Cavallo[1], David S. Wragg[1,2], Jonas Sottmann[3,4], Alexey Y. Koposov[1,5] and Helmer Fjellvåg[1].*

[1]Centre for Material Science and Nanotechnology, Department of Chemistry, University of Oslo, PO Box 1033, Blindern, N-0315, Oslo, Norway.

[2]Norwegian National Resource Centre for X-ray Diffraction and Scattering (RECX), Department of Chemistry, University of Oslo, PO Box 1033, Blindern, N-0315, Oslo, Norway.

[3]Sorbonne Université, CNRS, Physico-chimie des Électrolytes et Nanosystèmes Interfaciaux, PHENIX, F-75005 Paris, France.

[4]Réseau sur le Stockage Electrochimique de l'Energie (RS2E), FR CNRS 3459, 80039 Amiens Cedex, France.

[5]Department of Battery Technology, Institute for Energy Technology (IFE), Instituttveien 18, NO-2007 Kjeller, Norway.

*carmen.cavallo@smn.uio.no

Abstract

Progress in the field of Na-based batteries strongly relies on the development of new advanced materials. However, one of the main challenges of implementing new electrode materials is the understanding of their mechanisms (sodiation/desodiation) during electrochemical cycling. *Operando* studies provide extremely valuable insights into structural and chemical changes within different battery components during battery operation. The present review offers a critical summary of the *operando* X-ray based characterization techniques used to examine the structural and chemical transformations of the active materials in Na-ion, Na-air and Na-sulfur batteries during (de)sodiation. These methods provide structural and electronic information through diffraction, scattering, absorption and imaging or through a combination of these X-ray-based techniques. Challenges associated with cell design and data processing are also addressed herein. In addition, the present review provides a perspective on the future opportunities for these powerful techniques.

List of Acronyms

AI	Artificial intelligence
CT	Computed tomography
DEG-DME	Diethylene glycol dimethyl ether
DFT	Density functional theory
EDX	Energy dispersive X-ray spectroscopy
EXAFS	Extended X-ray absorption fine structure
FTIR	Fourier transform infrared spectroscopy
FWHM	Full width at half maximum
HAXPES	Hard X-ray photoelectron spectroscopy
LIB	Li-ion battery, lithium-ion battery
MCR-ALS	Multivariate curve resolution alternating least square
ML	Machine learning
NASICON	Na superionic conductor
NIB, SIB	Na-ion battery, sodium-ion battery
NMR	Nuclear magnetic resonance
PBA	Prussian blue analogues

PCA	Principle component analysis
PDF	Pair distribution function
PEEK	Polyether ether ketone
PTFE	Polytetrafluoroethylene
SAXS	Small-angle X-ray scattering
SEI	Solid electrolyte interface
SMS	Synchrotron Mossbauer spectroscopy
SOXPES	Soft X-ray photoelectron spectroscopy
TEG-DME	Tetraethylene glycol dimethyl ether
TMO	Transition metal oxides
TXM	Transmission X-ray microscopy
WAXS	Wide-angle X-ray scattering
XANES	X-ray absorption near-edge spectroscopy
XAS	X-ray absorption spectroscopy
XPS	X-ray photoelectron spectroscopy
XRD	X-ray diffraction
XRT	X-ray tomography

1. Introduction

Electrification of the energy sector represents a major challenge for society. Novel and powerful rechargeable batteries are an essential part of the solution. Li-ion batteries (LIBs) now dominate the market for transportation and portable electronics due to their high energy and power density [1, 2]. However, rapid growth of the LIB market may lead to shortage of some elements (including Li) currently utilized in LIBs, creating a need for complementary technologies. Non-aqueous Na-ion batteries (NIBs) are currently one of the most promising alternatives to LIBs representing a cheaper alternative, benefiting from the abundance of sodium in seawater and the earth's crust and its availability, which is not affected by geopolitical conflicts [3].

NIBs are inferior to LIBs in energy density, however, they are a potential competitor to LIBs for large-scale stationary storage [4] and applications where the lower cost of NIB's components becomes a significant factor. NIBs share the "rocking chair" principle of LIBs and benefited from the massive body of research on the latter. The larger size of Na^+ compared to Li^+ results in differences between the two chemistries: for example, graphite, which is the most common commercial anode in LIBs, does not work in the same way for NIBs [5, 6]. Other materials are better suited for NIBs than for LIBs, such as Sn [7], Cu_3PS_4 [8], Sb_2O_3 (better cycling stability) [9] and $NaNi_{1/2}Mn_{1/2}O_2$ (faster kinetics) [10]. For both chemistries, the electrodes have three main working principles: intercalation/insertion, conversion and alloying [11, 12]. Cathodes usually have intercalation or insertion mechanisms, while anode materials utilize all three working principles (either separate or combined). This review is focused on the use of X-ray based *operando* methods (already used extensively for LIBs and to some degree for NIBs [13-15]) for studying the chemical transformations of active materials during cycling of NIBs. Our review is not intended as an overview of materials for NIBs, as can be found in several recent reviews [1, 12, 16].

During the last decade, *operando* and *in situ* experiments became powerful tools for understanding the electrochemistry and associated structural changes of NIB materials during sodiation and desodiation.

10.1002/batt.202000294

In situ means "in the original place" and refers to measurements of materials in their working environment. In synthetic chemistry and catalysis, it is used to describe structural measurements conducted during chemical reactions, but for battery materials, *in situ* is used to describe any experiment where the material remains inside the battery cell (or another environment used for electrochemistry). This has led to some confusion in the literature, especially among those with long experience of *in situ* studies in other fields. The opposite term, *ex situ* ("off-site" or "away" from the site), indicates that the characterization has been performed on a material removed from a battery [14, 17, 18].

Operando is best translated to "in operation" and refers to measurements performed under operating/working conditions with activity data collected simultaneously. This implies that the measurements are conducted while the studied system is operated under conditions similar to a real application. For batteries, an *operando* experiment would involve logging electrochemical cycling data while simultaneously performing structural measurements with subsequent analysis linking the results together, as illustrated in Figure 1 [14, 17, 18]. This requires that the cycling continues during structural data collection, regardless of the C rate at which the battery is cycled. If the cycling is stopped while structural data are collected it becomes an *in situ* measurement. Based on more than 100 articles examined in the preparation of this review (Fig. S1), we observe that the use of the term *operando* has gradually surpassed that of *in situ* and other related terms for studies on batteries during cycling. We therefore use the term *operando* to describe all the studies in this review.

Generally, *ex situ* measurements can be performed using standard instruments and, therefore, are substantially more accessible than the alternatives mentioned above. However, in order to create a comprehensive set of *ex situ* data describing chemical transformations during cycling, many batteries must be fabricated and stopped at different stages of cycling. Furthermore, several problems can occur before the sample can be measured *ex situ*. First, an active material can immediately relax from its active state as soon as cycling stops. Second, careless disassembly of cells can lead to short circuits, contamination or damage to the material of interest. Third, *ex situ* measurements performed under ambient conditions, compromise the chemical integrity of the studied samples (e.g. NaBi and Na_3Bi formed through sodiation of Bi-based anodes rapidly decompose in air [19]). Finally, since only a few stages in the electrochemical process can reasonably be measured *ex situ*, it is easy to miss short-lived intermediates or unexpected non-linear behaviour of the chemical or structural transformations. The use of inert transfer chambers to preserve the sample while it is moved to the measurement instrument can further complicate *ex situ* measurements.

In situ and *operando* measurements do not require the removal of the studied materials from the battery, but they deliver their own disadvantages. Both types typically require the use of specially designed cells and equipment (see section 5 of the present review) [20-23]. Such set-ups often have limited comparability to conventional cells and require slow charge and discharge to obtain high quality structural data [24]. In addition, if high-energy radiation sources are used for data acquisition, heating and damage caused by the beam may affect the structure of the active material [25].

10.1002/batt.202000294

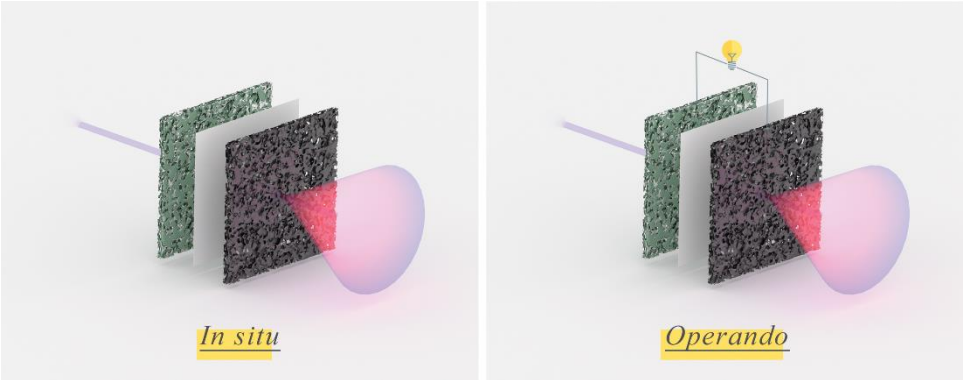

Figure 1. Scheme of in situ vs. operando experiments. Operando requires that the cycling is continuously performed and not stopped during the structural characterization.

Frequently, the active materials in NIBs undergo a complex series of transformations including formation of intermediate phases, which influence their overall stability and cyclability. It is exceptionally difficult to detect these intermediate states with conventional in situ and ex situ characterization methods due to relaxation from the active state. Operando methods open up the possibility of following the path of structural changes for active material while cycling, allowing detection of the intermediates and therefore determine the mechanism of functionality.

Operando studies using X-rays have been utilized from the early stages of battery research. Chianelli *et al.* reported what could be described as the first *operando* study of a battery material in 1978. The use of continuous X-ray diffraction to study of $LiTiS_2$-based cathode during cycling, with the structural data being correlated to the electrochemistry in the analysis, is described by the authors as "dynamic X-ray diffraction" [26]. It is noteworthy that this work was carried out only two years after Whittingham demonstrated a working rechargeable LIB with TiS_2 as the cathode [27], and 24 years before the term *operando* was popularised in the catalysis community [28-31]. As of today, a large ensemble of techniques used for *operando* characterization of batteries including diffraction/scattering, spectroscopy, imaging and combinations of these techniques. While several alternative techniques for *operando* studies, such as transmission electron microscopy (TEM), atomic force microscopy (AFM), nuclear magnetic resonance (NMR) and Raman spectroscopy, have become recently available, X-ray-based techniques are still the most popular choice in the battery research.

This review provides a summary of *operando* X-ray characterization techniques used for assessment of sodiation/desodiation mechanisms in NIBs. It is organized in three separate sections summarizing the most common *operando* X-ray techniques (diffraction/scattering, absorption/spectroscopy and imaging/combined techniques); and two more sections describing the design of *operando* cells and relevant data processing. It should be noted that some articles utilize several complementary techniques in the analysis of (de)sodiation mechanisms. Such results are grouped in this review according to the main operando technique used in the cited work.

2. X-ray diffraction and scattering

X-ray diffraction (XRD) is the most common and accessible technique for *operando* studies of batteries and battery materials. The basics of XRD is covered in several textbooks [32, 33] and, therefore, omitted from this review.

X-ray total scattering, or pair distribution function (PDF) analysis is less common than XRD and uses both diffuse elastic scattering (short-range order) and inelastic scattering (due to movement of atoms) in addition to the Bragg peaks. This methodology allows to obtain not only information about the long-range crystal structure (as with XRD), but also about the local structure. PDF is a powerful technique for studying amorphous battery materials [34].

Small-angle X-ray scattering (SAXS) utilizes the smallest angles in the X-ray scattering pattern (values of momentum transfer, q, < ~1 $Å^{-1}$). This provides information about size and shape of particles in a sample in the nm size range. SAXS is mainly used for characterizing porous materials or nanostructures with sizes in the range of 1-100 nm. The configuration of the SAXS instruments often allows the additional positioning of a regular XRD detector (often referred to as WAXS - wide angle scattering in the SAXS community) and thus SAXS is often combined with XRD.

The active materials in NIBs operate according to three main classes of mechanisms: intercalation/insertion, conversion and alloying. NIB cathode materials mainly operate through intercalation/insertion while a wide selection of anode materials utilize all three mechanism (separately or combined). The vast majority of materials used in NIBs are crystalline which makes XRD the most useful technique for *operando* characterization. These materials undergo a variety of phase transitions during (de)sodiation that are easy to observe through XRD. Some electrode materials, however, are amorphous or become amorphous during cycling (usually materials with alloying or conversion mechanisms). In these cases, techniques that do not rely on long range order such as SAXS, PDF and XAS can help to understand the operation mechanisms of amorphous materials.

A summary of the most recent *operando* studies using X-ray scattering and diffraction techniques used for Na-ion and Na metal batteries is shown in Table 1.

Table 1: Overview of scientific articles focused on operando X-ray diffraction and scattering. S = synchrotron, H = home laboratory, T = transmission (Debye-Scherrer) geometry, R = reflection (Bragg-Brentano) geometry.

Active material	**Type of material**	**Technique(s)**	**Cell type**	**X-ray window**	**S vs H**	**T vs R**	**Cycling rate**	**Acquisition time per scan**	**Ref.**
Sb	Alloying	XRD	Coin cell	Be	H		50 mA g^{-1}		[35]
Bi	Alloying	XRD	Coin cell	Kapton	H	T	50 mA g^{-1}		[19]
a-P/C	Alloying	WAXS, SAXS	Swagelok	Kapton	S	T	C/10	60 s	[36]
Bi_4Sb_4, Bi_2Sb_6	Alloying	XRD	Coin cell	Be	H		25 mA g^{-1}		[37]
$TiSb_2$	Alloying	XRD					C/30		[38]
Si	Alloying	XRD							[39]
P	Alloying	XRD/PDF-CT	Special/Tomography		S		C/2	7 min per slice	[40]
Bi	Alloying	XRD, TXM	Coin cell	Kapton	S			10 s	[41]
Bi	Alloying	XRD, XAS	Swagelok	Kapton	S	T	50 mA g^{-1}	2 min	[42]
Sb	Alloying	PDF	AMPIX		S		C/20	180 s	[43]
Hard carbon	Carbon	PDF	Capillary		S	T	C/10	4.5 min	[44]
Hard carbon	Carbon	XRD	Special	Be	H	R	C/25	1 h	[45]
Graphite	Carbon	XRD	Special	Al	H		30 mA g^{-1}		[46]
Graphite	Carbon	XRD	Special	Al	H		C/4-C/22		[47]
C (LCMH)	Carbon	XRD	Special	Kapton	H	R	100 mA g^{-1}	2.5 min	[48]

10.1002/batt.202000294

Graphite	Carbon	XRD	Coin cell	Kapton	S		20 mA g^{-1}	1 min	[49]
$CuSO_4$	Conversion	XRD							[50]
Cu_3PS_4	Conversion	XRD	Swagelok	Be	H	R	C/20	1 h	[8]
$(Ni_{0.5}Co_{0.5})_9S_8$@NC	Conversion	XRD	Coin cell	Kapton	H		100 mA g^{-1}		[51]
$Pb_3Nb_4O_{13}$	Conversion	XRD			H				[52]
$NiS_{1.03}$	Conversion	XRD		Be					[53]
Ni_3S_2	Conversion	XRD, TXM-XANES	Coin cell	Kapton	S				[54]
Co_3O_4	Conversion	XRD, SAXS, XAS	Coin cell	Kapton	S	T	0.1 C	5 s	[55]
$CoSe_2$	Conversion	XRD	Special	Be	H	R	100 mA g^{-1}	10 min	[56]
$NiSe_2$	Conversion	XRD	Special	Be	H	R			[57]
MoP	Conversion	XRD	Coin cell	Be	S				[58]
$Cu_{0.5}TiOPO_4$, $Fe_{0.5}TiOPO_4$	Conversion	XRD	Special	Be	H	R	16.9 mA g^{-1}		[59]
NiP_3	Conversion	XRD	Swagelok	Be	H		C/3		[60]
$FeSbO_4$	Conversion/ alloying	XRD	Special	Al	H	R	30 mA g^{-1}		[61]
SnS_2	Conversion/ alloying	XRD	Special		S		C/3		[62]
Sb_2O_3/rGO	Conversion/ alloying	XRD			H		C/5		[9]
Sb_2Se_3	Conversion/ alloying	XRD-XAS	Special	Be	H	R	100 mA g^{-1}	10 min	[63]
Bi_2S_3	Conversion/ alloying	XRD	Swagelok	Kapton	H, S	T	C/10	H: 20 min S: 1 min	[64]
$FeSb_2$	Conversion/ alloying	XRD	Swagelok	Be	H		C/6		[65]
$FeSb_2$	Conversion/ alloying	XRD	Coin cell	Kapton	H	R	C/50→ C/200→C /40→C/120→C/30	4 h	[66]
$Na_{2/3}Ni_{1/3}Mn_{2/3}O_{2-x}F_x$	Layered	XRD	El-Cell	Kapton	H		C/10-C/20		[67]
$Na_{0.66}Li_{0.22}Ru_{0.78}O_2$	Layered	XRD		Al	H				[68]
$Na_{0.67}Mn_{0.6}Fe_{0.25}Co_{0.15}O_2$ + $Na_2C_6O_6$	Layered	XRD	Special	Be	H	R	C/20	1 h	[69]
$Na[Ni_{0.60}Fe_{0.25}Mn_{0.15}]O_2$	Layered	XRD	Special	Al	H		C/10		[70]
Na_xMnO_2	Layered	XRD	Special		H	R	C/20	30 min	[71]
$Li_{0.5}Na_{0.4}CoO_2$	Layered	XRD	Swagelok	Kapton	H	R	20 μV s^{-1}		[72]
$Li_{0.2}NaMn_{0.8}O_2$	Layered	XRD							[73]
$NaMn_{0.33}Fe_{0.33}Ni_{0.33}O_2$	Layered	XRD							[74]
$Na_{2/3}Mn_{0.8}Fe_{0.1}Ti_{0.1}O_2$	Layered	XRD	Swagelok	Be	S	T	26-526 mA g^{-1}	40 s	[75]
$Na_{1.5}Li_{0.5}IrO_3$	Layered	XRD	Swagelok	Be	H		C/20		[76]
$Na_{2/3}[Ni_{1/3}Mn_{2/3}]O_2$	Layered	XRD	Special	Be	H	R	5 mA g^{-1}		[77]

10.1002/batt.202000294

$Na_{2/3}[Ni_{1/6}Mn_{1/2}Fe_{1/3}]O_2$									
$Na_{2/3}Ni_{1/6}Mn_{2/3}Cu_{1/9}Mg_{1/18}O_2$	Layered	XRD	Swagelok	Al	H		C/10		[78]
$Na_{0.7}Mn_{0.8}Mg_{0.2}O_2$	Layered	XRD	Coin cell	Kapton	S	T	15 mA g^{-1}	3.5 min	[79]
$Na_{2/3}Ni_{1/3}Mn_{2/3}O_2$	Layered	XRD			S		C/2		[80]
$Na_{0.67}Mn_{0.65}Ni_{0.2}Co_{0.15}O_2$, $Na_{0.67}Mn_{0.65}Ni_{0.2}Mg_{0.15}O_2$	Layered	XRD	Coin cell		H		30 mA g^{-1}		[81]
$Na_{0.67}Mn_{0.5}Fe_{0.5}O_2$ (MgO coated)	Layered	XRD					0.2 mV s^{-1}		[82]
$Na_xNi_{0.3}Mn_{0.7}O_2$	Layered	XRD	Coin cell		H	R	15 mA g^{-1}	20 min	[83]
Na(TM)O_2	Layered	XRD	Swagelok	Be	H		C/50, C/10	1 h	[84]
$Na_{1.2}Ni_{0.2}Mn_{0.2}Ru_{0.4}O_2$	Layered	XRD	Swagelok		H		C/12		[85]
$Na_{0.67}Mn_{0.6}Fe_{0.25}Al_{0.15}O_2$	Layered	XRD	Special	Be	H	R	C/13	1 h	[86]
$Na_{0.6}Li_{0.2}Mn_{0.8}O_2$	Layered	XRD			H, S	R, T	H: C/30 S: C/5	H: 2h S: 5 min	[87]
$NaFe_{0.25}Mn_{0.25}Ni_{0.25}Ti_{0.25}O_2$	Layered	XRD		Al	H		0.4 C		[88]
$Na[Li_{0.05}Ni_{0.3}Mn_{0.5}Cu_{0.1}Mg_{0.05}]O_2$	Layered	XRD	Swagelok	Al	H		C/10		[89]
$Na_{0.9}Ca_{0.05}Ni_{1/3}Fe_{1/3}Mn_{1/3}O_2$	Layered	XRD			S		C/10		[90]
$Na_3Ni_2SbO_6$	Layered	XRD	Swagelok	Al	H		C/20		[91]
MoO_3	Layered	XRD	Capillary		S	T		2.4-3.4 min	[92]
$Na_{2/3}Ni_{1/3-x}Fe_xTi_{2/3}O_2$	Layered	XRD	Coin cell	Be	H		15 mA g^{-1}	3.2 min	[93]
$NaNi_{2/3}Sb_{1/3}O_2$	Layered	XRD		Be	H		C/5	15 min	[94]
$Na_{2/3}Ni_{1/4}Mn_{2/3}Cu_{1/12}O_2$	Layered	XRD		Be	H		C/40		[95]
$NaNiO_2$	Layered	XRD, TXM-XANES	Coin cell	Kapton	S	T	C/10	3 s	[96]
$NaNi_{0.5}Cu_{0.05}Mn_{0.4}Ti_{0.1}O_2$	Layered	XRD	Special	Al	H				[97]
$NaNiMn_{0.5-x}Ti_xO_2$ ($0 \leq x \leq 0.5$)	Layered	XRD	Swagelok	Al	H		C/20	30 min	[98]
$NaNi_{1/3}Fe_{1/3}Mn_{1/3}O_2$	Layered	XRD	Coin cell	Kapton	S	T			[99]
NbS_2	Layered	XRD	Special	Be	H	R	100 mA g^{-1}	12.5 min	[100]

10.1002/batt.202000294

$NaFe_{1/2}Co_{1/2}O_2$	Layered	XRD					6 mAg^{-1}	35 min	[101]
$NaFe_{1/3}Ni_{1/3}Ti_{1/3}O_2$	Layered	XRD	Special	Be	H	R	0.1 mV s^{-1}	63 min	[102]
$Na_{2.55}V_6O_{16}$*0.6H_2O	Layered	XRD	Special	Al	H	R	10 mA g^{-1}		[103]
$Na_{0.7}Fe_{0.4}Mn_{0.4}Co_{0.2}O_2$	Layered	XRD	Capillary		S		40-80 mA g^{-1}	25.7 s	[104]
$Na_xMn_{1/3}Fe_{2/3}O_2$	Layered	XRD, XANES	Special	Be	H		C/80	1 h	[105]
$Na_{0.9}Cu_{0.22}Fe_{0.30}Mn_{0.48}O_2$	Layered	XRD	Special	Al	H		C/10		[106]
$Na_{0.67}Mn_{0.8}Mg_{0.2}O_2$	Layered	XRD	Coin cell		S	T	12 and 100 mA g^{-1}	4.4 s	[107]
$Na_{0.67}[Mn_{0.5}Fe_{0.5}]O_2$, $Na_{0.67}[Mn_{0.65}Ni_{0.15}Fe_{0.2}]O_2$	Layered	XRD	Special		H	R	13 mA g^{-1}	30 s	[108]
$Na_{0.84}Fe_{0.56}Mn_{0.44}O_2$	Layered	XRD	Special	Graphite	H	R	0.08C and 0.17C	18 min	[109]
$NaNiO_2$	Layered	XRD	Special	Be	H		C/70	20 min	[110]
Na_xVO_2	Layered	XRD	Special	Be	H		C/100	1 h	[111]
$NaCrO_2$	Layered	XRD	Special		S		C/12		[112]
$Na_{0.44}Co_{0.1}Mn_{0.9}O_2$	Layered and Network	XRD	Swagelok	Al	H				[113]
O_2 + CoO/CoP	Na-O2	XRD			S		200 mA g^{-1}		[114]
O_2	Na-O2	XRD	Special	Kapton	S	T	0.075 mA cm^{-2}	10 s	[115]
O_2	Na-O_2	XRD	Special	Polymide	H	R	0.2 mA cm^{-2}		[116]
S	Na-S	XRD	Coin cell	Kapton	S	T			[117]
$Na_3MnTi(PO_4)_3$/C@rGO	Network	XRD		Be	H		50 mA g^{-1}	120 s	[118]
$Na_{3+x}Mn_xV_{2-x}(PO_4)_3$ ($0\leq x\leq 1$, $\Delta x=0.2$)	Network	XRD		Be, Sapphire	H, S		C/8, C/5		[119]
$Na_4Co_3(PO_4)_2P_2O_7$	Network	XRD	Special		H				[120]
$Na_4MnV(PO_4)_3$	Network	XRD	Swagelok	Be	H		1 Na^+/10 h	55 min	[121]
$NaTiOPO_4$	Network	XRD	Special	Be	H		C/50	11 min	[122]
$Na_3(VO)Fe(PO_4)_2F$	Network	XRD, XANES	Swagelok	Be	S		C/10		[123]
$Na_3V_2O_2(PO_4)_2F$	Network	XRD	Special	Sapphire	S	T	C/5	10 s	[124]
$Na_2Fe_2(SO_4)_3$@C@GO	Network	XRD	Coin cell		S	T	50 mA g^{-1}		[125]
$Na_2Co_2(SeO_3)_3$	Network	XRD	Special		H	R	5 mA g^{-1}	30 min	[126]
TiO_2	Network	SAXS	Coin cell	Polyimide	S	T	C/12 and 1C	0.6 s*30	[127]
$Na_4MnV(PO_4)_3$	Network	XRD	Special	Sapphire	S	T	C/4		[128]
$NaFePO_4$	Network	XRD	Special	Be	H, S	R, T	C/60 and C/20, 1C	H: 30 min S: 2.3 min	[129]

$Na_3(VOPO_4)_2F$	Network	XRD	Special		H, S	T	C/10, C/6		[130]
$Na_7V_3Al(P_2O_7)_4(PO_4)$	Network	XRD	Swagelok	Be	H		C/20	1 h	[131]
$Na_3V_2(PO_4)_2FO_2$	Network	XRD	Special		H	R	C/40	2 h	[132]
$Na_3VCr(PO_4)_3$	Network	XRD	Coin cell	Kapton	S	T	C/10	14-15 min	[133]
$Na_{1.86}Fe_3(PO_4)_3$	Network	XRD	Swagelok	Be	H		C/10 and C/20		[134]
Gd_2TiO_5	Network	XRD	Coin cell	Kapton	S	T	4 mA g^{-1}	6.38 min	[135]
$Na[FeTi]O_4$	Network	XRD	Swagelok	Be	H		C/10	37 min	[136]
$Na_3V_2O_{2x}(PO_4)_2F_{3-2x}$	Network	XRD	Coin cell	Kapton	S	T	C/2	4 min	[137]
$NaFePO_4$	Network	XRD	Special	Be	H	R	2.4 mA g^{-1}	9 min	[138]
Na_xFePO_4	Network	XRD	Swagelok	Be	S	T	$1Na^+/23$ h	2 s $scan^{-1}$	[139]
$Li_4Ti_5O_{12}$	Network	XRD	Special	Mylar	S			15 min	[140]
$Na_3V_2(PO_4)_3$, Bi (full cell)	Network, Alloying	XRD							[141]
$Na_xMn_{1-2y}Sn_yFe(CN)_6$	PBA	XRD	Swagelok	Be	H		C/20		[142]
$Na_xMnFe(CN)_6$	PBA	XRD			H		60 mAh g^{-1}		[143]
$Na_{1.34}Ni[Fe(CN)_6]_{0.81}$	PBA	XRD			H		20 mAh g^{-1}		[144]
$NaFeFe(CN)_6$	PBA	XRD	Coin cell	Kapton	S	T	10 mA g^{-1}		[145]
$Na_{1.32}Mn[Fe(CN)_6]_{0.83}\cdot zH_2O$	PBA	XRD, XANES	Swagelok	Kapton	S	T	C/10	7 min	[146]
$Fe[Fe(CN)_6]_{1-x}$, $FeCo(CN)_6$	PBA	XRD	Coin cell	Kapton	S	T	0.05-0.2 mA	4.36 min	[147]

2.1 Layered intercalation materials

Operando XRD is the perfect technique for studying intercalation compounds. During cycling, the materials usually stay crystalline and undergo minor structural changes (volumetric changes and phase transitions), which are readily followed by XRD. *Operando* methods have therefore been deployed by several authors to detect the intermediate phases forming during sodiation/desodiation. Layered transition metal oxide (TMO) cathode materials are popular in NIBs due to their low Na^+ diffusion barriers. They have the general formula of Na_xMO_2, where M is one or more transition metals (with a few exceptions) and through tuning of the lattice structure and chemical composition excellent Na-host materials can be obtained [148]. Layered cathode materials frequently form structures based on edge shared MO_6 octahedra organized in layers that can intercalate Na-ions in either prismatic or octahedral sites. The transition metal ions are oxidised and reduced during sodiation and desodiation. Delmas *et al.* [149] proposed a widely used classification system for the Na_xMO_2 materials based on the geometry of the Na sites (P for prismatic or O for octahedral) and the number of distinct MO_2 layers that form the stacking sequence. These materials can exhibit quite complex behaviour during cycling, because it is possible to change the stacking pattern with small shifts to adjacent MO_2 layers. This behaviour is strongly dependent on the chemical composition. The complexity and

diversity of mechanisms found for this group of materials is difficult to predict from their compositions, or to infer from electrochemical data, and *operando* XRD has been crucial in revealing how their functionality is linked to their structure.

These layered materials can be divided into two subgroups based on the as synthesised structure: those with a pristine O3 phase and those with a pristine P2 phase. Fully sodiated materials (x = 1 in Na_xMO_2) usually crystallise as O3-type phases, while sodium deficient materials (often x = 2/3) generally form P2-type phases [150, 151]. During desodiation the O3 and P2 structures often transition to the related P3 and O2 structures, respectively; a series of operando studies, summarized below, revealed and confirmed these mechanisms. General crystal structures with O3, P3, P2 and O2 stacking sequences are shown in Figure 2 [152].

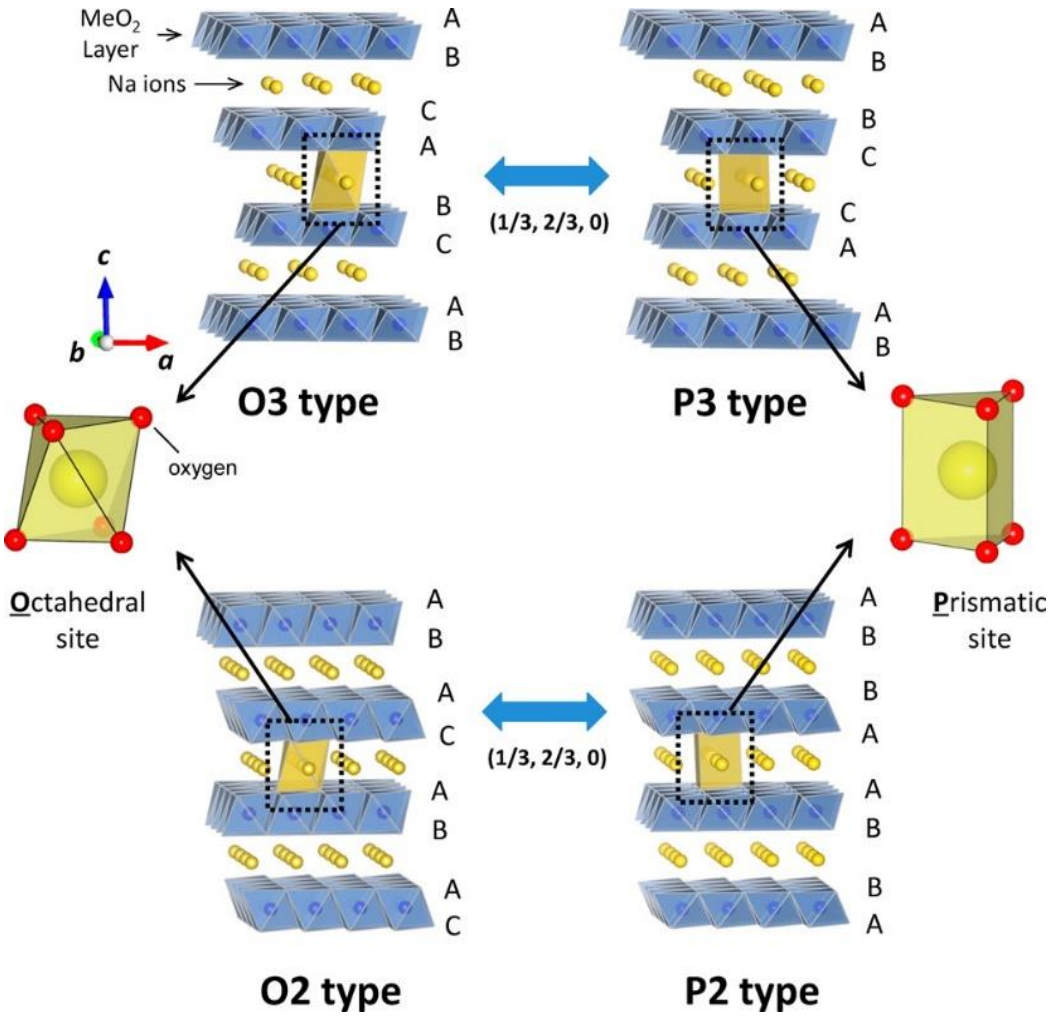

Figure 2. Layered O3, P3, O2 and P2 crystal structures with their respective stacking sequences. The blue and yellow spheres represent the transition metal and Na^+ ions in the O-type frameworks, respectively. Adapted from [152].

Xie *et al.* demonstrated an O3-P3-O3 transition by *operando* XRD during cycling of $NaNi_{1/3}Fe_{1/3}Mn_{1/3}O_2$ up to 4.0 V (Figure 3a) [99]. Cycling to higher voltages (4.3 V) leads to different behaviour: above 4 V, the P3 phase transforms further into a monoclinic distorted O3' phase, Figure 3b. During discharge from 4.3 V, the O3' phase transforms into a monoclinic distorted P3' phase before reverting to the initial, hexagonal O3 phase. Similar behaviour has been reported by Ding *et al.* for $Na[Ni_{0.6}Fe_{0.25}Mn_{0.15}]O_2$ [70]. However, this material transitions

10.1002/batt.202000294

from O3 to P3 *via* an intermediate O'3 (monoclinic) phase. Above 4.0 V, the P3 phase transitions into a second hexagonal O3 phase (denoted O3''). This process is reversible and only the initial O3 phase was detected at end of discharge, as shown in Figure 3c-f. However, the full phase transition to O3'' lead to capacity degradation over time, and for long term stability it was beneficial to lower the cut-off voltage to 4.0 V. These two examples of materials with similar compositions show that these mechanisms cannot be generalized, as they are so sensitive to the combination of cations in the Na_xMO_2 structure. Several materials, including $NaFe_{0.25}Mn_{0.25}Ni_{0.25}Ti_{0.25}O_2$ [88], $Na_xMn_{1/3}Fe_{2/3}O_2$ (x = 0.77) [105] and $NaNi_{2/3}Sb_{1/3}O_2$ [94], have also been reported to form O1 phases at high voltages, often in combination with P3. The complexity of the observed transformations particularly emphasizes the necessity of operando studies as the only method that can clearly reveal the important intermediate phases forming during (de)sodiation processes. The knowledge of the intermediates and when they are formed allows to explain the stability and cyclability of studied material and thus, provide further guidelines for material's improvements. There are several good examples where the results from operando XRD has been used to improve the cyclability of a material by implementing small changes. For example by controlling the potential window or coating the materials [70, 74, 90].

10.1002/batt.202000294

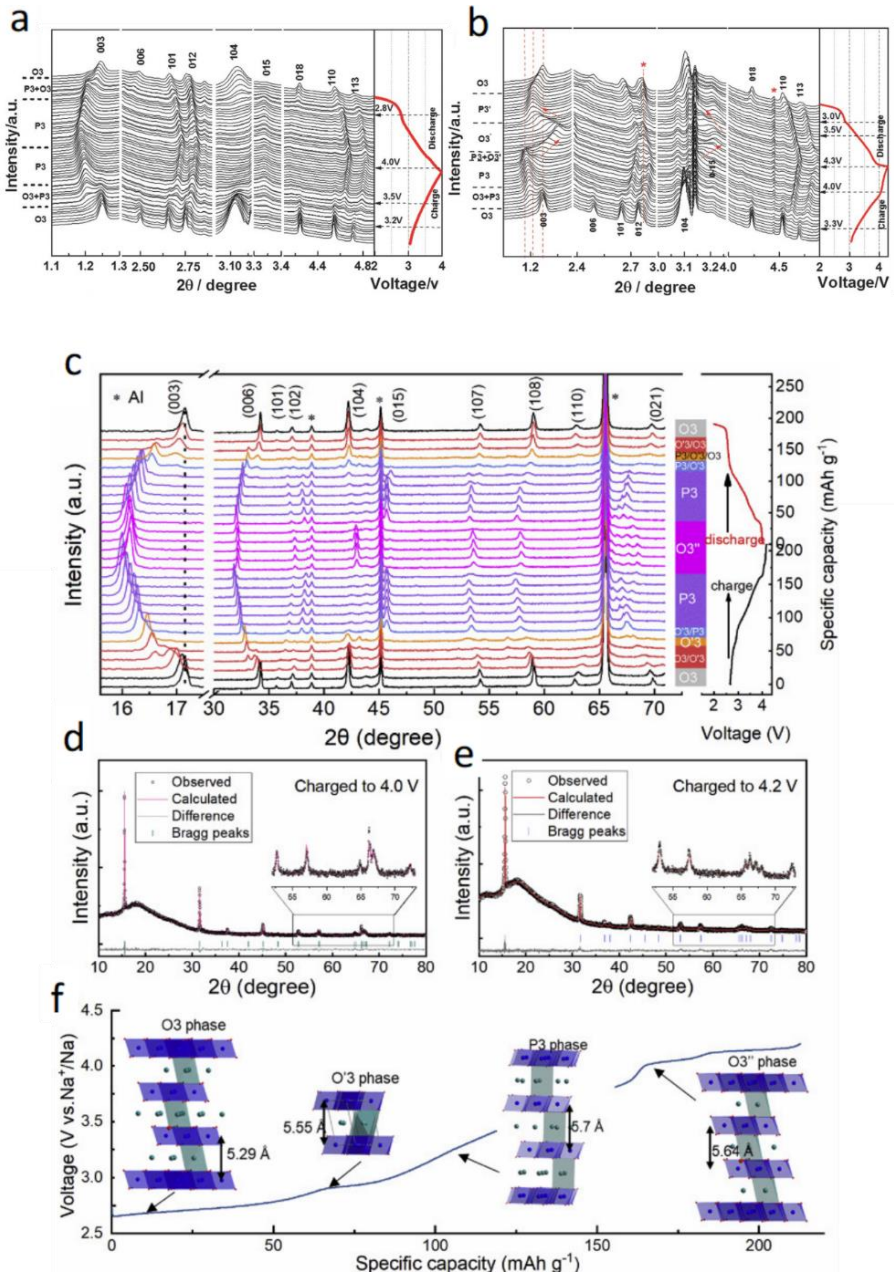

Figure 3: Operando XRD patterns collected from the first cycle of $Na_{1-\delta}Ni_{1/3}Fe_{1/3}Mn_{1/3}O_2$ electrode (a) between 2.0 and 4.0 V and (b) between 2.0 and 4.3 V. Adapted from [99]. (c) Operando XRD patterns collected during the first cycle of $Na_{1-x}Ni_{0.65}Fe_{0.25}Mn_{0.15}O_2$ in Na half-cell within the voltage range of 2.0–4.2 V. Corresponding phases and charge-discharge curves are given on the right side. (d) and (e) Rietveld refinement patterns of powder XRD data for O3-NNFM cathode charged to 4.0 V and 4.2 V. (f) Crystal structure evolution of O3-NNFM during desodiation. Adapted from [70].

Operando XRD also revealed that P2 materials can follow several different structural routes during cycling. Some maintain their structure during cycling (solid solution behaviour) [73, 81, 82, 87], others reversibly transition into O2 phases [69, 80, 86, 104], a third group stop at disordered intermediate phases termed "Z-"or "OP4" [68, 77, 83, 95]. Jung *et al.* showed an example of the P2-O2-P2 transition for $Na_{0.7}Fe_{0.4}Mn_{0.4}Co_{0.2}O_2$, where the plateaus and slopes in the voltage plots clearly correspond to phase changes and lattice parameter variations respectively in the XRD data (Figure 4) [104].

10.1002/batt.202000294

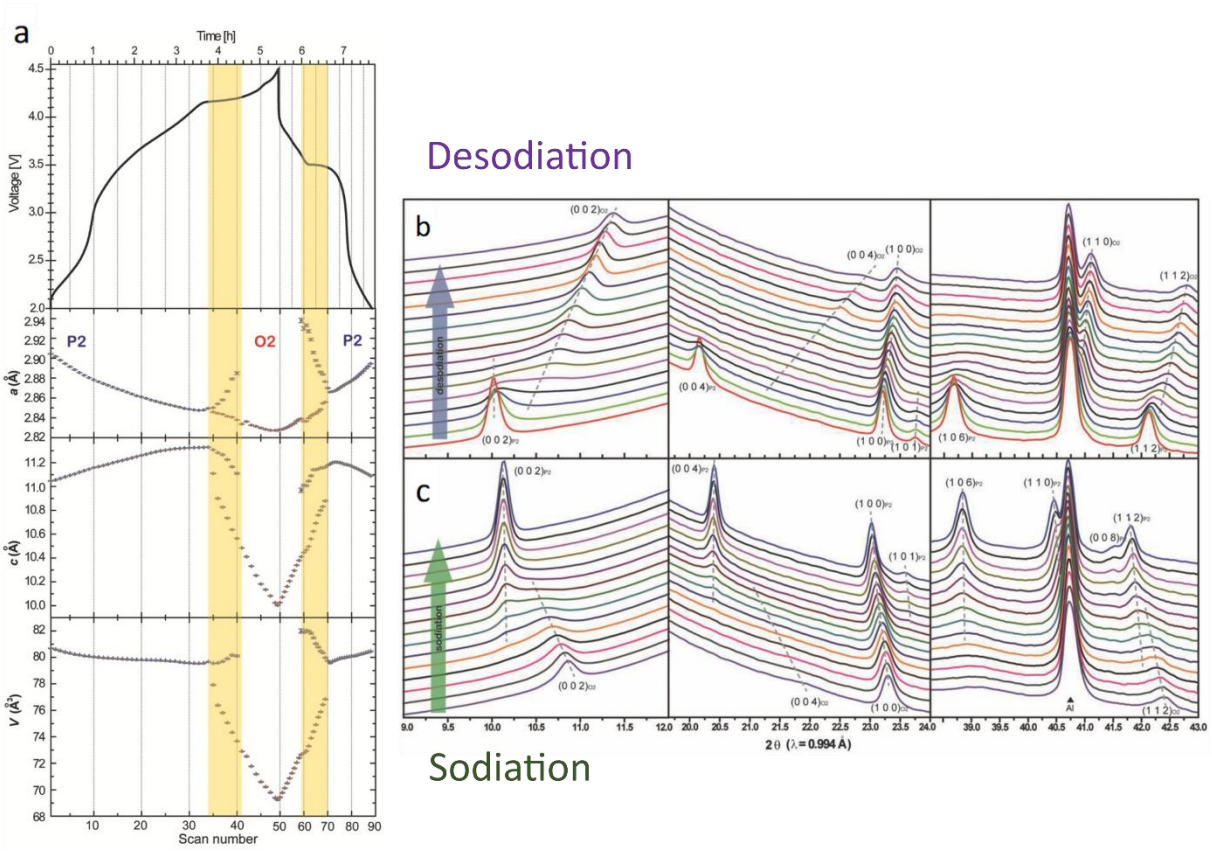

Figure 4: a) Charge discharge curves and the corresponding evolution of cell parameters and phases of the P2–$Na_{0.7}Fe_{0.4}Mn_{0.4}Co_{0.2}O_2$ electrode extracted from operando synchrotron XRD patterns (b) desodiation and (c) sodiation. Adapted from [104].

Sommerville *et al.* studied the Z phase in detail and described it as an intergrowth of P- and O-type layers [77]. The OP4 phase is an ordered case of the Z-phase with a 50:50 intergrowth in which the P- and O-type layers alternate, as shown in Figure 5a. This study demonstrated that $Na_{2/3}[Ni_{1/6}Mn_{1/2}Fe_{1/3}]O_2$ transitions from the P2 phase through the Z phase and reaches the OP4 phase at around 4.3 V, as shown in **Error! Reference source not found.**b-e. $Na_{0.66}Li_{0.22}Ru_{0.78}O_2$ [68] and $Na_xNi_{0.3}Mn_{0.7}O_2$ [83] display similar behaviour, with the P2 phase reversibly transforming to the Z phase. These operando studies not only established the nature of the Z phase, but also explained its effect on the stability of the material during cycling: when transitioning through the Z phase the material undergoes less abrupt volumetric changes and thus the capacity retention is improved.

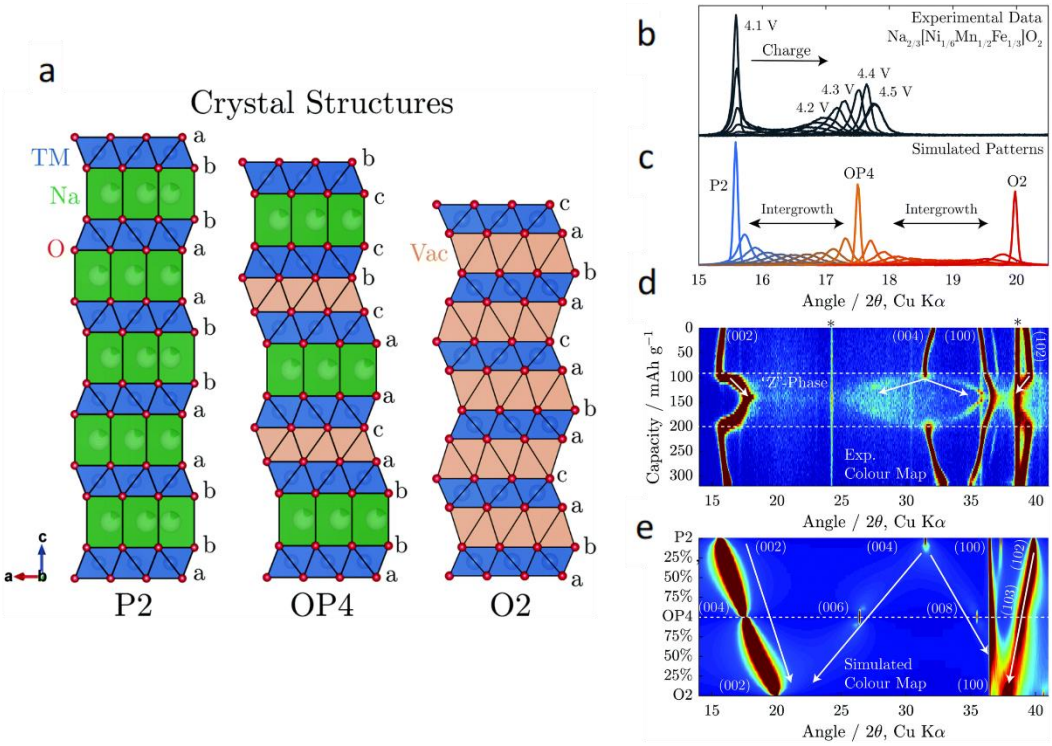

Figure 5: (a) Illustration of the P2, OP4 and O2 phases showing the correlation between the structures. (b) Experimental diffraction patterns at different voltages during the operando study of $Na_{2/3}[Ni_{1/6}Mn_{1/2}Fe_{1/3}]O_2$. (c) Simulated diffraction patterns by using FAULTS for intergrowth structures composed of P2 and OP4, and OP4 and O2. (d) Experimental diffraction data over a wider 2θ range as a colour map. (e) Simulated diffraction data as a colour map. Adapted from [77].

2.2 Insertion network materials

The most common three dimensional (3D) structured sodium insertion materials are polyanionic compounds (including NASICON), titanates (TiO_2, $Li_4Ti_5O_{12}$ and Gd_2TiO_5) and Prussian blue analogues.

Polyanionic frameworks include phosphates, fluorophosphates and sulphates and are typically composed of XO_4 tetrahedra or trigonal XO_3 (X = P, S), and MO_6 octahedra (where M is 3d transition metal). NASICON-type materials (such as $Na_3V_2(PO_4)_3$), $NaFePO_4$ and $Na_2Fe_2(SO_4)_3$ are among the most promising cathode materials in this group. $NaFePO_4$ with the maricite structure has shown a capacity of 142 mAh g^{-1} and a capacity retention of 95 % after 200 cycles [153]. This is significantly better than olivine structured $NaFePO_4$, which has a capacity of 125 mAh g^{-1} and slightly worse cycling stability [154]. The olivine $NaFePO_4$ materials, have an average voltage around 3.0 V [155]. $Na_2Fe_2(SO_4)_3$ is among the most promising sulfates for NIBs. In a composite with graphene oxide, $Na_2Fe_2(SO_4)_3$ demonstrates a capacity of approximately 100 mAh g^{-1}, stability for several hundred cycles, and an average voltage around 3.8 V [125].

Several groups showed that olivine $NaFePO_4$ exhibits a different behaviour than the well-studied olivine analogue of $LiFePO_4$. Instead of one well-defined, two-phase transition (as for $LiFePO_4$), Na_xFePO_4 undergoes phase transitions with several intermediate phases revealed by *operando* XRD, and with more contribution from solid solution regions [129, 138, 139]. Furthermore, such studies allowed the determination of different sodiation and desodiation mechanisms for the material [138]. In comparison to orthophosphates, the pyrophosphates exhibit

a higher redox potentials for active elements, however, mass of the active material also increases with such substitution lowering the specific capacity [131]. In the case of Co-based compounds: $Na_xCo_3(PO_4)_2P_2O_7$ [120], a series of redox reactions occur between 4.3 and 4.7 V. This increased chemical complexity of the material results in several phase transitions during cycling, as demonstrated by *operando* XRD.

The NASICON-type compounds represent an interesting sub-group of phosphate materials. For the typical NASICON-type material, $Na_3V_2(PO_4)_3$, the structure consists of corner shared VO_6 octahedra and PO_4 tetrahedra. This gives a structure with several 3D channels for fast intercalation of Na^+ [16]. This compound shows a capacity slightly above 100 mAh g^{-1} and a stable voltage plateau at 3.4 V. It has good cycle life and excellent rate capabilities where a capacity above 100 mAh g^{-1} can be maintained even at 2 A g^{-1} [141]. Unfortunately, vanadium compounds are toxic. Hence, replacing this with more benign elements is an important research target. To reflect that, Zakharkin *et al.* studied a series of $Na_{3+x}Mn_xV_{2-x}(PO_4)_3$ (x = 0, 0.2, 0.4, 0.6, 0.8 and 1) with *operando* XRD [119, 128]. They showed that increased amount of Mn in the structure leads to small capacity improvements and more solid solution type behaviour. Pure vanadate materials clearly show a two-phase mechanism (Figure 6) [119]. The phase transitions in $Na_4MnV(PO_4)_3$ are highly dependent on the cut-off voltage. The transition from the monoclinic to the rhombohedral phase is reversible when charged to 3.8 V, but becomes irreversible when charged to 4.0 V [128]. A similar study by Chen *et al.* [121] supports this finding. Several *operando* XRD studies on fluorinated NASICON-type materials with general formula $Na_3V_2O_{2x}(PO_4)_2F_{3-2x}$ ($0 \leq x \leq 1$) were also reported [124, 130, 132, 137]. These materials demonstrate higher redox potentials than the non-fluorinated materials and good reversibility even when charged up to high voltages (4.3 V).

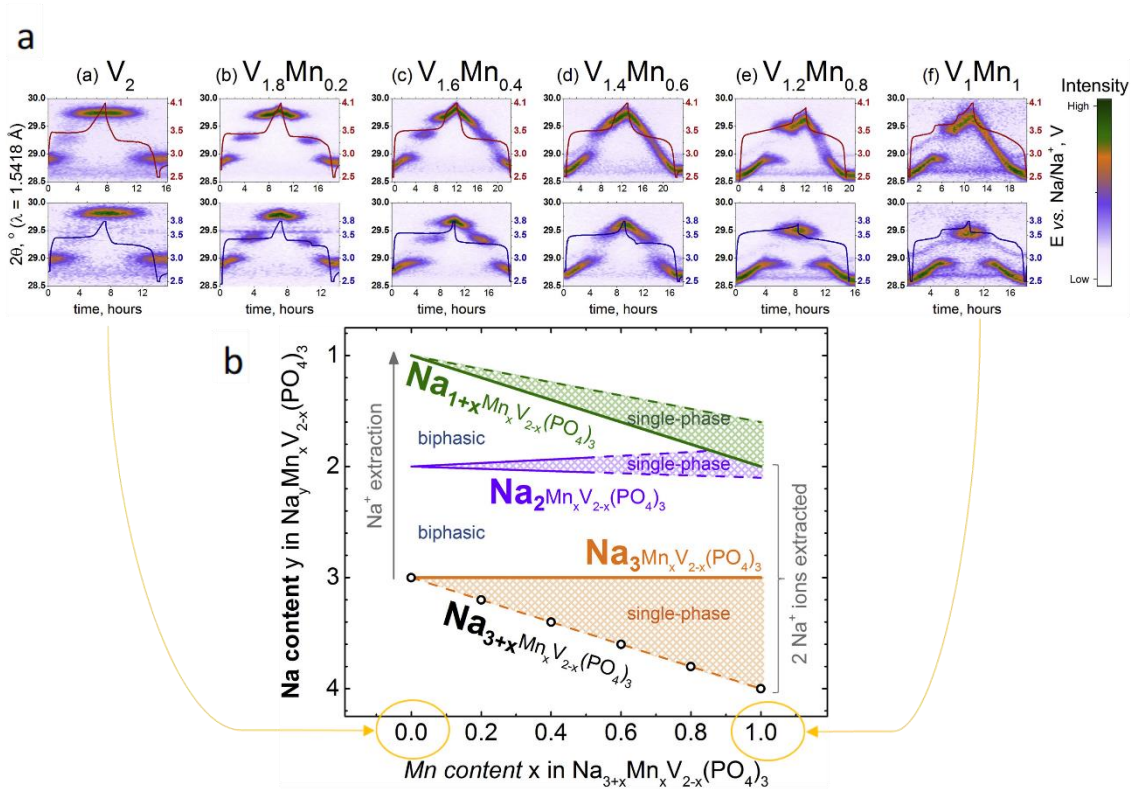

Figure 6: a) Operando XRD study on $Na_{3+x}Mn_xV_2(PO_4)_3$ with 5 different values of x with and increment of 0.2. The figure shows a selected region (024 reflection, 28.5–30.0°, CuKα1/Kα2) of XRD patterns during (de)sodiation in the 2.5–3.8 V

(bottom) and 2.5-4.1 V (top) voltage windows. b) Schematic illustration of the desodiation mechanisms based on the data from (a). Adopted from [119].

Prussian blue analogues (PBAs) have the general formula $A_xMM'(CN)_6 \cdot nH_2O$, where the A is a guest ion such as Na^+, K^+, Ca^{2+}, Mg^{2+} or a molecule of H_2O, M and M′ are transition metals and the ambidentate CN- ligands bridge the two metals M and M' in a corner-sharing octahedral configuration [156]. This class of materials has great potential as cathode materials for NIBs, due to the large voids into which Na^+ can be inserted. PBAs also deliver good reversibility during (de)sodiation and, therefore, excellent cycling stability. However, their cubic crystal structure can be easily distorted by varying the level of water and CN^- vacancies. An *operando* XRD study on cubic and monoclinic $Na_xMnFe(CN)_6$ by Tang *et al.* showed that the monoclinic version goes through several phase changes (monoclinic – cubic – tetragonal), which makes it unstable under cycling [143]. The cubic phase, in contrast, maintains its structure during cycling, giving superior cycling stability. Several studies of other PBA modifications confirmed that the cubic phase has superior cycling stability relative to the distorted versions [142, 146]. However, a study of rhombohedral $Na_{1.34}Ni[Fe(CN)_6]_{0.81}$ showed that the material goes through a highly reversible two-phase reaction from rhombohedral at low voltages to cubic at high voltages, which also gives great cycling stability [144]. $Na_xFeFe(CN)_6$ and $Na_xFeCo(CN)_6$ were also studied with *operando* XRD showing only minor structural changes during cycling [145, 147].

Unlike the insertion materials discussed above, titanates are used as anodes rather than cathodes in NIBs. They are of interest due to their exceptional cycling stability. Santoro *et al.* performed an *operando* SAXS study on TiO_2 nanoparticles, showing that the particle size is preserved during cycling while the mean distance between the secondary nanoparticles changes [127]. This is a rate-dependent phenomenon; at a low rate (C/12) the nanoparticles homogeneously drift apart, while at a higher rate (1C) nanoparticle aggregation is the dominant factor. *Operando* XRD was also utilized to demonstrate that titanate anodes such as Gd_2TiO_5 [135], $Na_x[FeTi]O_4$ [136] and $Li_4Ti_5O_{12}$ [140] display very small structural and volumetric changes upon (de)sodiation, leading to good cycling stability.

2.3 Carbon materials

In the vast plethora of anode materials for NIBs, hard carbons are popular due to their low cost, high capacity and cycling stability [157]. However, the amorphous nature of hard carbons limits the information that could be obtained by *operando* XRD. In such materials sodiation and desodiation result in a slight shift of the main broad diffraction peak, due to expansion and contraction [45, 48]. SAXS is a powerful tool for the study of hard carbon, able to detect the total porosity, (i.e., the surface (open) porosity, as well as the bulk (closed) porosity). However, the use of *operando* SAXS is far from routine in battery characterization, probably due to the scarcity of lab-scale SAXS instruments [158]. Therefore, complementary techniques are needed to study these materials in detail.

Stevens and Dahn [150, 160] were the first to attempt *operando* XRD and SAXS on carbon materials to study the intercalation of alkali metal ions. The historical model of sodium insertion into micropores was proposed after they conducted *operando* SAXS on sugar-derived hard carbons and observed a clear change in intensity of the SAXS signal. Alvin *et al.* revealed the mechanism of Na^+ cycling in hard carbon using a range of techniques including XRD, SAXS and Raman spectroscopy [161].

PDF analysis of total scattering data is a powerful technique for studying hard carbon materials, since it allows the study of amorphous compounds. Mathiesen et al. [44] successfully used *operando* PDF to study hard carbon (de)sodiation mechanisms. They observed changes to the interatomic distances both interplane and intraplane depending on the state of charge. They also showed an increasing level of disorder in the structure during cycling.

Although it is the most common anode for LIBs, graphite is a bad host material for Na^+-ions with low preference for intercalation. Graphite anodes for NIBs have nevertheless been studied with *operando* XRD. In this case, the use of diethylene glycol dimethyl ether (DEG-DME), and other "glymes", as electrolytes enabled intercalation of solvated Na^+-ions into graphite. Kim *et al.* reported one of the first studies, where they used a 1 M $NaPF_6$ in diethylene glycol dimethyl ether (DEG-DME) as electrolyte. *Operando* XRD revealed the structural evolution of the graphite during the solvated Na^+ intercalation [49]. Further detailed *operando* XRD studies of the staging mechanism of solvated Na^+ into graphite were conducted, demonstrating sodium content of up to NaC_{18} [46, 47].

A few other studies reported *operando* X-ray-based techniques [162, 163] for studying (de)sodiation mechanisms in carbon materials in NIBs. However, these are not discussed in this review, as the *operando* data were complementary to other techniques and were not a key part of the findings.

2.4 Conversion and alloying materials

Most conversion and alloying materials undergo a complex set of structural and chemical transformations during cycling. These are not always visible in conventional *ex situ* characterization. *Operando* XRD revealed the mechanisms of cycling for several conversion and alloying NIB anode materials and for some materials that combine these working mechanisms. Some conversion and alloying materials are poorly suited for conventional XRD due to their amorphous nature or formation of amorphous phases during cycling. In these cases, the PDF technique can offer some hope for structural analysis.

Alloying anode materials for NIBs are generally composed of elements from the p-block of the periodic table (Sb, Sn, Bi, Si and P) or alloys composed of these elements (BiSb, $TiSb_2$). The sodiation of these materials often proceeds through formation of multiple crystalline phases, which can be tracked using *operando* XRD. For instance, several *operando* XRD studies performed on Bi alloying anodes confirmed the reversibility of Bi transitions to NaBi and Na_3Bi upon sodiation [19, 41, 141]. The structure of Na_3Bi formed during cycling depends on the starting crystallite size of Bi. Nanosized Bi transforms into cubic Na_3Bi upon sodiation, while sodiation of larger Bi particles results in the formation of hexagonal Na_3Bi [42]. The structure of the Na_3Bi phase affects the cycling stability, in which the cubic form is superior to the hexagonal form. A similar Na alloying mechanism was also proposed for BiSb-alloys based on *operando* XRD [37]. However, elemental Sb has different cycling behaviour than Bi. Initially, Gao *et al.* demonstrated that Sb alloys with Cu from the current collector as well as Na, forming $Na_3Cu_xSb_{1-x}$ [35]. There is no evidence of a crystalline NaSb phase, but a detailed PDF study combined with *ex situ* nuclear magnetic resonance (NMR), conducted by Allan *et al.*, demonstrated the formation of several amorphous phases upon cycling [43]. As shown in Figure 7 a-c, there are three different amorphous phases ($Na_{1.7}Sb$, $Na_{1.0}Sb$ and $Na_{3-x}Sb$) in addition to the two crystalline phases (Sb and Na_3Sb). The study also showed the formation of amorphous $Na_{3-x}Sb$ only during sodiation, while desodiation follows a different pathway.

10.1002/batt.202000294

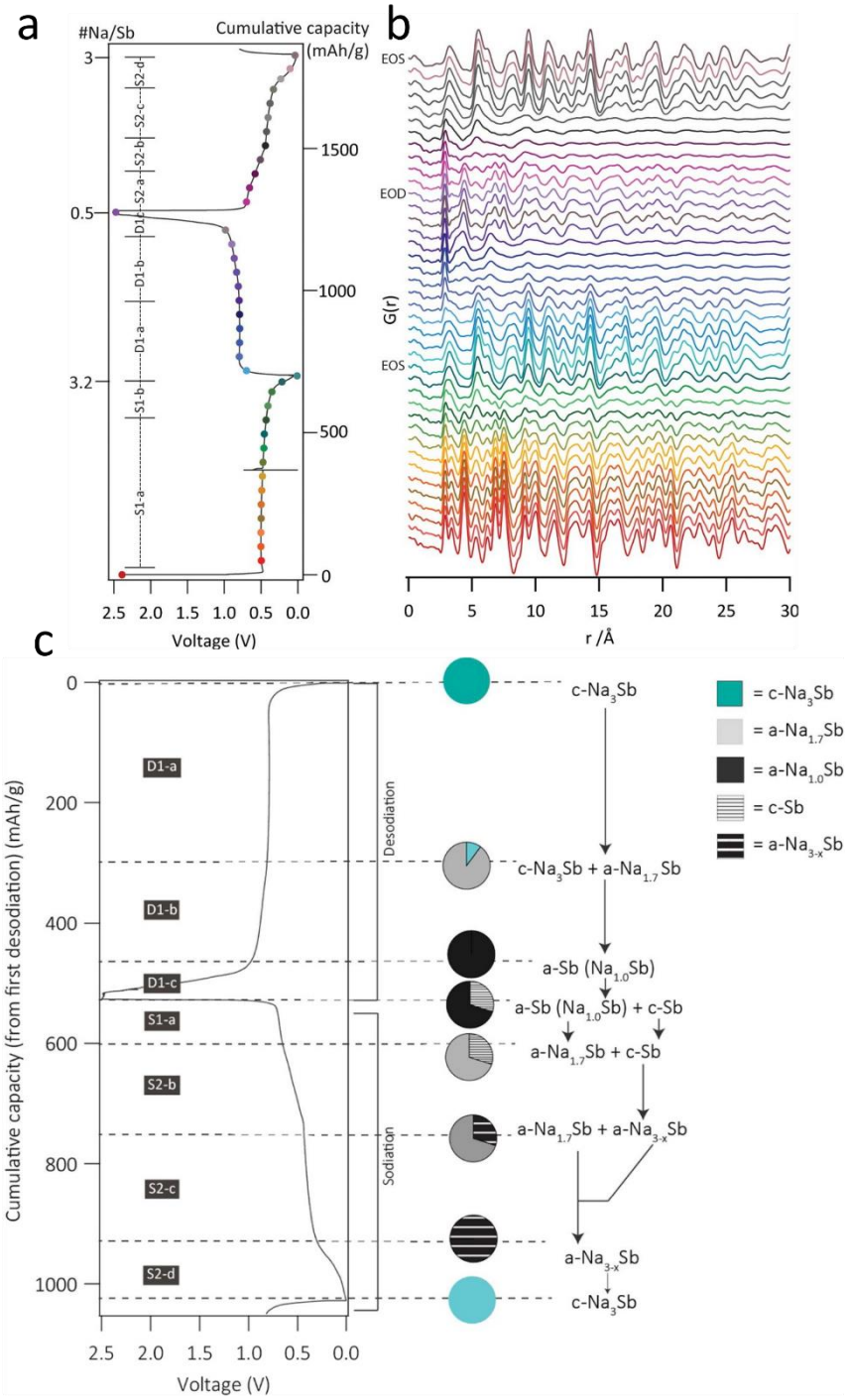

Figure 7: (a) charge-discharge curves and (b) corresponding PDF graphs obtained from operando PDF measurements of Sb electrode during the operando PDF measurements. c) (de)sodiation mechanisms of Sb derived from the operando PDF measurements from the first desodiation and the second sodiation with a cycling rate of C/20. Adapted and Reproduced from [43]*. Copyright [2016] American Chemical Society.*

A notable difference between sodiation and desodiation pathways were also observed for phosphorus alloying anodes, using *operando* SAXS/WAXS and PDF-CT [36, 40]. These studies demonstrated that the sodiation of P-based electrodes follows the thermodynamic path *via* NaP to Na_3P, while during desodiation, the material takes a different pathway through the metastable $Na_{2.6}P$ and $Na_{2.36}P$ phases (desodiated forms of Na_3P) and directly back to amorphous P without

forming NaP. The *operando* PDF study also demonstrated an enormous change in the crystallite size of phosphorous during cycling, which changes from 10 nm when P is fully sodiated to around 1 nm when fully desodiated [40]. This study clearly illustrates the importance of *operando* studies for elucidation of (de)sodiation pathways that are not typically visible through conventional *ex situ* characterization.

Si is a very promising alloying material for LIBs but does not perform well in NIBs. Through nanostructuring of Si it is currently possible to obtain stable capacities slightly above 400 mAh g^{-1} [39], which is significantly less than for other alloying materials such as Sn and Sb (typical capacities around 600 mAh g^{-1} over at least 100 cycles) [164, 165]. An *operando* XRD study on nanocrystalline Si in NIBs showed a transformation into an amorphous phase upon sodiation [39]. However, the sodiation mechanism in Si remains to be evaluated.

Conversion NIB anodes are of particular interest due to their high specific capacities. The materials undergo a reaction where the elements in the electrode material separate and Na binds to the most electronegative element. The general reaction is given by

$$Na^+ + e^- + MX \rightarrow M + NaX$$

Where M is a transition metal (Fe, Ni, Co, Cu) and X is an electronegative non-metal (F, O, S, N, P, Se). Understanding the conversion process is extremely important for the rational design of future materials in this class. Thus, *operando* methods are particularly suitable for the task. To illustrate that, Ou *et al.* studied $CoSe_2$ and $NiSe_2$ with *operando* XRD. $NiSe_2$ showed a conversion reaction forming amorphous Ni-nanoparticles embedded in Na_2Se, with Na_xNiSe_2 as an intermediate [57]. This reaction mechanism was confirmed through *operando* XRD and *ex situ* TEM. $CoSe_2$ showed similar behaviour by going through a two-step conversion reaction to CoSe and Co-metal with the formation of Na_2Se in both steps. The first step forming CoSe is quite reversible, while the full conversion to Co is difficult to reverse [56]. Hollow spheres of $NiS_{1.03}$ [53], microcrystals of Ni_3S_2 [54], $(Ni_{0.5}Co_{0.5})_9S_8$ nanoparticles embedded in nitrogen-doped porous carbon shells [51], powders of NiP_3 [60] and nanorods of MoP [58] showed similar behaviour; the clusters of the transition metals are formed together with Na_2S or Na_3P. Many conversion materials also show signs of amorphous phases formation during cycling, which could be further studied with techniques other than XRD. For example, Xu *et al.* studied Co_3O_4 with *operando* XRD, SAXS and XANES, showing transformation of Co_3O_4 into an amorphous phase during the conversion reaction [55]. More complex conversion materials such as Cu_3PS_4 [8], $CuSO_4$ [50], $Pb_3Nb_4O_{13}$ [52], $Fe_{0.5}TiOPO_4$ and $Cu_{0.5}TiOPO_4$ [59] were also studied with *operando* XRD and generally show the same behaviour.

The replacement of the transition metals in oxides and chalcogenides with more electronegative p-block elements (Sn, Sb and Bi) provides materials that combine conversion and alloying mechanisms. SnS_2 [62], Bi_2S_3 [64], Sb_2O_3/rGO [9] and Sb_2Se_3/rGO [63] were studied by *operando* XRD confirming combined conversion and alloying as a sodiation mechanism. Such mechanism consists of initial conversion of the starting material into a stable matrix of sodium oxide, sulphide or selenide with embedded (nano)particles of Sn, Bi or Sb. In subsequent cycles, the embedded particles are reversibly sodiated through alloying process. The conversion part of the reaction is only reversible at relatively high voltages (around 2 V for both Bi_2S_3 and Sb_2Se_3/rGO), meaning that it would be difficult to utilize this extra capacity in a full cell. Reversal of the initial conversion also negatively affects the cycling stability. The combined mechanism can also be achieved in alloys of transition metals with a p-block metal or similar

mixed oxides. Examples are $FeSb_2$ [65, 66] and $FeSbO_4$ [61], where Fe forms an electrochemically inactive amorphous phase during sodiation that helps to improve the cycling stability of the material driven by Sb – Na_3Sb alloying reaction.

2.5 Sulfur, air and Na metal batteries

Most *operando* studies on Na-based batteries in the literature are focused on NIBs. However, there are a few studies on Na-air, Na-S and Na-metal batteries. An *operando* XRD study performed by Pinedo *et al.* showed a different reaction mechanism for Na-air battery when cycling with dry O_2 compared to wet O_2. NaO_2 was the sole discharge product under dry conditions, while in wet conditions $Na_2O_2{\cdot}2H_2O$ and NaOH are formed [116]. One of the major challenges in assessing the performance of Na–O_2 batteries is to understand the parasitic reactions that occur during cycling. Therefore, it is important to characterize and quantify the materials formed during cell operation and correlate these processes to the charge accumulated during discharge/charge. In response to this challenge, Liu *et al.* performed *operando* XRD with an internal Si standard to quantify the formation of crystalline NaO_2 in a Na-air battery during the first discharge [115]. The most recent *operando* study on Na-air batteries performed by Wang *et al.*, elucidated the presence of Na_2O_2, NaOH and Na_2CO_3 in the first cycle for a battery containing a CoO/CoP catalyst [114]. To the best of our knowledge, only one *operando* XRD study has been performed on Na-S batteries, illustrating sodiation progress through the following phase transitions: $S_8 \rightarrow Na_2S_x \rightarrow Na_2S_4 \rightarrow Na_2S$ (x = 8, 6, and 5). On desodiation, most of the S_8 phase is recovered, but over many cycles, nonconductive Na_2S accumulates leading to irreversible capacity loss [117].

3. X-ray absorption and spectroscopy.

X-ray absorption spectroscopy (XAS) is frequently used in *operando* studies of specific elements in battery materials. Electrons in the different energy levels of the atom are excited at characteristic photon energies measured in terms of intensity changes at the so called absorption edges. The X-ray energies are scanned across the "edge" of the target element. Usually, *operando* XAS experiments concentrate on just a single absorption edge, although with the optimized setup multiple edges can be probed reasonably fast [166].

The XAS spectrum can be split into regions before, close to and after the adsorption edge. X-ray absorption near edge spectroscopy (XANES) uses a small region close to (and including) one of the main absorption edges in the XAS-spectrum. From the energy and fine structure of the absorption edge, information about the oxidation state of the elements as it varies during cycling can be extracted. Information about element's site symmetry and electronic structure can also be extracted from the XANES region (which includes the so-called "pre-edge" region just below the absorption edge). Extended X-ray absorption fine structure (EXAFS) uses the energy range from approximately 50 eV to >600 eV above the absorption edge. EXAFS provides information about short-range order around the absorbing atom in the material: type, number and distribution of neighbouring atoms. In general, EXAFS analysis requires data with much better quality compared to XANES. A challenge with EXAFS analysis is the complexity of an average of a number of local structures that may change during the course of the cycling reactions. The active elements in NIB electrodes change their oxidation state and/or undergo chemical transformations during cycling. XAS can track these changes in crystalline or amorphous materials providing information on the local environment of a specific element. XAS becomes an especially strong tool when combined with other *operando* techniques.

Several synchrotron beamlines are capable of preforming such experiments, revealing the structural and electrochemical mechanisms that occur during cycling. Examples of *operando* XAS studies on NIB materials are summarized in Table 2.

Table 2: Overview of scientific articles on operando X-ray absorption and spectroscopy techniques (XAS, EXAFS, XANES, XPS). S = synchrotron, H = home laboratory, T = transmission (Debye-Scherrer) geometry, F = fluorescence geometry.

Active material	**Type of Material**	**Technique(s)**	**Cell type**	**X-ray window**	**S vs H**	**T vs F**	**Cycling rate**	**Acquisition time per scan**	**Ref.**
$CuSO_4$	Conversion	XANES, EXAFS							[50]
SnO_2	Conversion	XANES, EXAFS	Special	Glassy carbon	S	F	C/30 and C/40		[167]
Co_3O_4	Conversion	XANES, EXAFS	Coin cell	Kapton	S	T	0.2 C	4 min	[55]
Bi_2O_3	Conversion	XANES							[168]
Na_xCoO_2 (thin film)	Conversion	XPS	Special		H			2 h	[169]
Bi_2S_3	Conversion/ alloying	XANES, EXAFS	Swagelok	Kapton	S, H	T	C/10	2-7 min	[64]
$FeSb_2$	Conversion/ alloying	XANES, EXAFS	Swagelok	Be	S	T	C/2 and C/5		[170]
$BiVO_4$, $Bi_2(MoO_4)_3$	Conversion/ alloying	XANES	Swagelok	Kapton	S	T	C/10	2 min	[171]
$NaNi_{1/3}Fe_{1/3}Mn_{1/3}O_2$	Layered	XANES	Coin cell	Kapton	S	T			[99]
$Na_{0.85}Li_{0.17}Ni_{0.21}Mn_{0.64}O_2$	Layered	XANES, EXAFS	Pouch cell	Aluminzed Mylar	S	T			[166]
$Na_xMn_{1/3}Fe_{2/3}O_2$	Layered	XANES	Coin cell	Polyimide	S		C/50	30 min	[105]
$Na_3V_2(PO_4)_2F_3$	Network	XANES	Special	Kapton	S	F	C/10	4 min	[172]
$Na_3V_2(PO_4)_3$	Network	XANES, EXAFS	Pouch cell	Triplex	S	T	C/15	29 min	[173]
$Na_3(VO)Fe(PO_4)_2F_3$	Network	XANES			S	T	C/10	6 min	[123]
$NaFePO_4$	Network	XANES	Coin cell	Kapton	S	T			[174]
$Na_{1.32}Mn[Fe(CN)_6]_{0.83}\cdot z H_2O$	PBA	XANES	Swagelok	Kapton	S	T	C/10	3 min	[146]

An early *operando* XAS study of battery materials was reported by Pivko *et al.* in 2012 [173]. They compared two stable modifications of the $A_3V_2(PO_4)_3$ framework (A= Li, Na) by monitoring the vanadium oxidation states with V K-edge XANES and changes in the local environment of vanadium in $Na_3V_2(PO_4)_3$ during the first charge and discharge with V K-edge EXAFS. They showed that the average valence state of vanadium changes reversibly from $V^{3.0+}$ to $V^{3.8+}$ during cycling. In addition, a reversible structural deformation was observed, demonstrating the stability of $Na_3V_2(PO_4)_3$ for high-energy-density batteries.

Sodium−vanadium fluorophosphate compounds $Na_3V_2(PO_4)_2F_{3-y}O_y$ (with y ranging from 0 to 2) are among the most promising polyanionic compounds for the use in NIBs [175]. These materials were extensively studied by a number of methods including *operando* XAS. Broux *et al.* [172] used *operando* XANES combined with solid-state NMR to confirm the disproportionation of V^{4+} into V^{3+} and V^{5+}, which occurs upon the extraction of one Na^+ ion from $Na_3V_2(PO_4)_2F_3$. The K edge XANES unambiguously confirmed that this phenomenon does not occur at the end of charging, but happens immediately after the extraction of one Na^+

ion, i.e., after reaching the composition $Na_2V^{III}V^{IV}(PO_4)_2F_3$ (shown Figure 8a-b and 8c) [172]. The same research group also reported the substitution of V^{4+} with Fe^{3+} in $Na_3V_2(PO_4)_2F_2$ accompanied by subsequent *operando* studies [123]. *Operando* XANES combined with EXAFS, Mossbauer and solid-state NMR revealed that V^{4+} is completely oxidized to V^{5+} during the reversible single Na^+ extraction (in the voltage window from 2.5-4.3 V *vs.* Na^+/Na). Moreover, *operando* synchrotron XRD revealed that Na^+-vacancy ordering during desodiation does not occur. This is the opposite of the behaviour previously reported for $Na_3V_2(PO_4)_2F_3$ and $Na_3(VO)_2(PO_4)_2F$ [124].

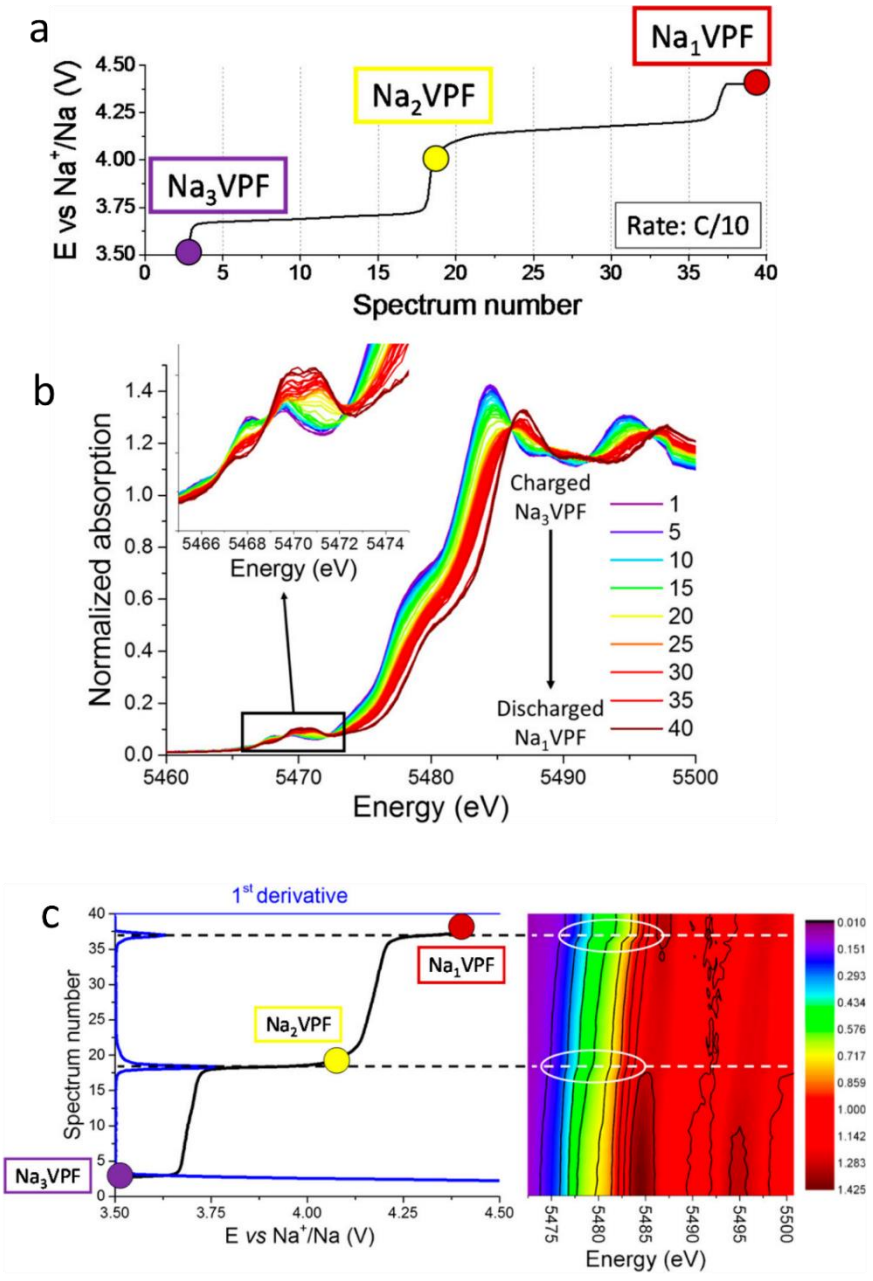

Figure 8: a) Voltage as a function of the time (spectrum number) obtained from operando XAS measurement during the first galvanostatic desodiation of $Na_3V_2(PO_4)_2F_3$ at C/10. b) Evolution of the vanadium K edge during desodiation obtained from operando XANES. The inset is focused on the pre-edge region c) Left: voltage (black line) as a function of the spectrum number (same as a)) with the associated first derivative (blue line). Right: 2D projection of the corresponding operando vanadium K edge XANES spectra emphasizing discontinuities at voltage jumps. Reprinted (adapted) with permission from [172]. Copyright (2017) American Chemical Society.

Layered oxides, extensively discussed in section 2, have also been studied by *operando* XAS. Karan *et al*. investigated the Na^+ cycling mechanism in P2-type $Na_{0.85}Li_{0.17}Ni_{0.21}Mn_{0.64}O_2$ based on the similarity between $LiMO_2$ and $NaMO_2$ [166]. Using a custom-made electrochemical cell for *operando* XAS to study the Ni and Mn edges, they demonstrated that Ni reversibly changes it's oxidation states from Ni^{2+} to Ni^{3+} and Ni^{4+} while Mn^{4+} is electrochemically inactive. For materials where primary transition metal is partially substituted, *operando* XAS is the technique of choice allowing to assess the electrochemical functionality of each metal. For instance, the addition of Fe could rebalance the stoichiometry of Ni and Mn elements, resulting in a special class of layered TMO materials [176, 177]. By employing *operando* XANES combined with *operando* Mössbauer spectroscopy, Mortemard de Boisse *et al.* demonstrated that the Fe^{3+}/Fe^{4+} couple is active at high voltages while the Mn^{4+}/Mn^{3+} couple is electrochemically active at low voltages and high sodium contents: $x > 0.67$ in $Na_xMn_{1/3}Fe_{2/3}O_2$ [105].
Operando quasi-simultaneous XRD combined with XAS provide insight to the redox activity of PBA materials in NIBs. Sottmann *et al.* [146] studied the (de)sodiation mechanism in $Na_{1.32}Mn[Fe(CN)_6]_{0.83}\cdot zH_2O$ with z = 3.0 (monoclinic) or 2.2 (cubic). The monoclinic and cubic versions show similar redox behaviour for the Fe^{3+}/Fe^{2+} couple, but the cubic structure better utilizes the redox reactions of the Mn^{3+}/Mn^{2+} couple and, therefore, shows superior cycling stability. However, during cycling Mn in the active material is lost as $NaMnCl_3$ due to reaction with the $NaClO_4$ electrolyte, which causes capacity degradation. Moreover, the capacity loss is pushed by the coordinated water in $[Fe(CN)_6]$ vacancies and higher zeolitic water content in the pristine material.
Sb K-edge XAS and synchrotron Mössbauer spectroscopy (SMS) were combined for the first time to clarify the roles of iron and antimony in the electrochemical reaction mechanism of an $FeSb_2$ NIB anode [170]. The study observed the formation of amorphous Na_3Sb and Fe nanoparticles containing a small fraction of Sb ($\leq 10\%$) in their lattice. After the first discharge, the amorphous/nanoconfined Sb is the active material leading to an alloy-type mechanism rather than a conversion reaction. Both *operando* and *ex situ* XAS were used to confirm the incomplete conversion and alloying reaction that SnO_2 undergoes during sodiation , due to the formation of a dense NaO_2 layer [167]. Lee *et al.* identified the mechanism of the conversion reaction of $CuSO_4$ in a NIB using *operando* XANES and EXAFS. They discovered that during the initial charging/discharging, the oxidation states varies between Cu^{2+} and metallic Cu^0. The simultaneous dissociation of the Cu–O bond and formation of the metallic Cu–Cu bond during initial discharging was confirmed from the Fourier transform of the EXAFS spectra [37].
Cobalt oxide was studied with *operando* EXAFS by Xu et al. [55], supported by complementary *operando* X-ray based characterizations. They confirmed the conversion of Co_3O_4 to Co and Na_2O upon sodiation. Compared with the lithiation process, the cobalt oxide undergoes smaller changes in pore structure, oxidation state, crystal structure and local structure during sodiation, which is attributed to the intrinsic low sodiation activity of Co_3O_4.

Operando X-ray photoelectron spectroscopy (XPS) is not widely deployed due to the complexity of the cell design required. To the best of our knowledge, the first *operando* XPS study on oxide-based NIBs electrodes was conducted by Guhl *et al.* [169]. A novel cell setup was used to study the sodiation mechanism during charging of a Na_xCoO_2/NASICON/Na battery half-cell NIB. The *operando* study validates the results obtained through *ex situ* analysis, which suggested the oxidation of Co^{3+} to Co^{4+} [169].

4. X-ray microscopy (TXM and STXM) and tomography (XRT and CT).

X-ray microscopy can be used to image samples by detecting reflected or transmitted X-rays. Full-field transmission X-ray microscopy (TXM) or scanning transmission X-ray microscopy

(STXM) are two main techniques in X-ray microscopy. To assess chemical information about the sample TXM uses XAS or SAXS data while STXM uses energy dispersive X-ray spectroscopy (EDX), Auger spectroscopy and other methods commonly used for scanning electron microscopy (SEM). TXM and STXM allow imaging of thicker samples than is possible with electrons, with lower radiation damage however with sacrifice of resolution (maximum of around 10 nm) [178]. Higher resolution (around 5 nm) can be achieved in coherent STXM by using ptychography [179-182].

Tomographic reconstruction methods can be used on imaging data to create 3D models of battery components and particles. They can be applied to X-ray radiography [183], microscopy [7] or space resolved diffraction/scattering [184, 185] and microfocus XAS data [186]. Examples of imaging techniques used for *operando* studies of battery materials are shown in Table 3.

Table 3: An overview of scientific articles on operando X-ray imaging and combined X-ray techniques used on sodium ion batteries. S = synchrotron, H = home laboratory, T = transmission (Debye-Scherrer) geometry.

Active material	**Type of material**	**Techniques**	**Cell type**	**X-ray window**	**S vs H**	**T**	**Cycling rate**	**Acquisition time**	**Ref.**
Sn	Alloying	XRT, TXM	Coin cell	Kapton	S	T	5 mA g^{-1}	10 s	[7]
Bi	Alloying	TXM-XRD	Coin cell	Kapton	S	T		60 s	[41]
P	Alloying	XRD/PDF-CT	Special/Tomography		S	T	C/2	7 min per slice	[40]
FeS	Conversion	TXM-XANES	Coin cell	Kapton	S	T		10 s	[187]
Ni_3S_2	Conversion	TXM-XANES	Coin cell	Kapton	S	T	C/10	15 s	[54]
CuO	Conversion	TXM-XANES	Coin cell		S	T		10 s	[188]
$NaNi_{1/3}Fe_{1/3}Mn_{1/3}O_2$	Layered	TXM-XANES	Coin cell	Kapton	S	T		20 s	[99]
$NaNiO_2$	Layered	TXM-XANES	Coin cell	Kapton	S	T	C/10	20 s	[96]

Xie *et al.* analysed the phase transformation of $NaNi_{1/3}Fe_{1/3}Mn_{1/3}O_2$ during Na-ion intercalation through *operando* TXM combined with XRD [99]. A non-equilibrium solid-solution reaction occurs during desodiation, while during sodiation, the XRD patterns suggest that the phase transformation of $Na_{1-\delta}Ni_{1/3}Fe_{1/3}Mn_{1/3}O_2$ follows a reversible O3–P3–O3 sequence during cycling. Finally, *ex situ* XANES shows that only the Ni^{2+}/Ni^{3+} redox couple is electrochemically active between 2.0 and 4.0 V, while Ni^{3+}/Ni^{4+} and Fe^{3+}/Fe^{4+} are active between 4.0 and 4.3 V. By combining these techniques, they monitored both the structural and the morphological changes of the particles, creating chemical maps of a region in the sample showing the phase changes.

The same techniques were used to reveal the electrochemical behaviour of $NaNiO_2$ (Figure 9) [96]. Two phase transitions ($NaNiO_2$ – Na_xNiO_2 – $Na_{0.19}NiO_2$) were detected during the cycling process and phase sensitive imaging showed that the changes spread from the outer shell to the core of the particles during both sodiation and desodiation (Figure 9 f and g).

10.1002/batt.202000294

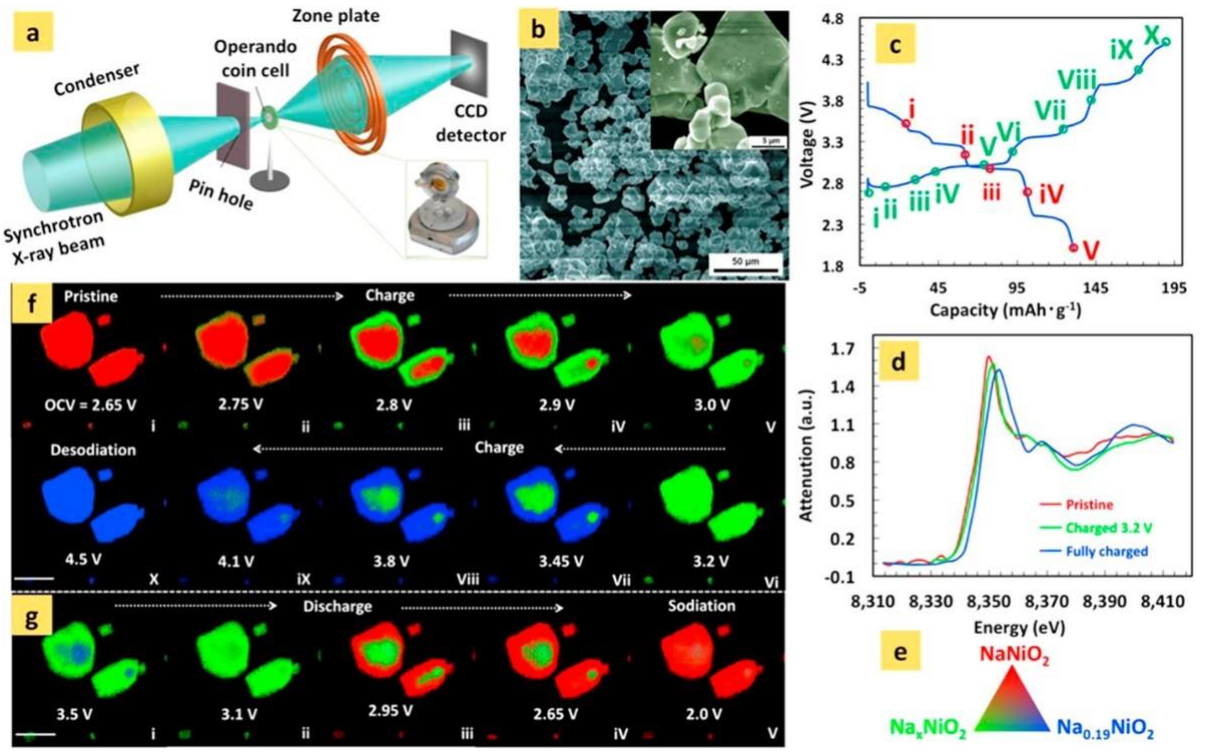

Figure 9: Operando hard X-ray spectro-imaging of two-dimensional microstructural evolution of $NaNiO_2$ cathode. (a) Schematic illustration of the TXM experimental setup. (b) Scanning electron micrographs of the $NaNiO_2$. Inset is the magnified graph of the NaNiO2. (c) Charge and discharge profiles of the operando cell. The cell was cycled at the rate of 1/10 C between 2.0 V and 4.5 V. The small circles correspond to the states of charge where the data were collected and fitted as chemical mapping. (d) Reference XANES spectra selected from three different operando charged states. (e) The reference colour indicates the three phases in the chemical mapping. (f) and (g) are the two-dimensional chemical phase mapping during the first charge and discharge process. Scale bar: 10 µm. Reprinted with permission from [96].

The same group further explored the use of a TXM microscope, combining it with XANES analysis, to elucidate the Na^+ cycling mechanism of FeS through mapping of the chemical phase transformation [187]. Similar to $NaNiO_2$, sodiation spreads gradually from the surface into the core of the particles, in a partially irreversible process.

While the surface-to-core sodiation patterns commonly observed in *operando* TXM-XANES studies could be predicted, experiments also show that the formation of core-shell structures during sodiation do not indicate the same mechanism for all materials. For instance, in CuO [188], the sodiation happens only in the surface layers and the core becomes inactive (immobilized) to the sodiation. In Ni_3S_2 [54], the sodiation first occurs in the outer regions of the particles and gradually proceeds into the core. However, the sodiation of the core leads to volume expansion and particle cracking ultimately increasing the surface area. This process opens desodiation pathways through the cracked particles. The analysis reveals another reason for the high irreversible capacity of this material: while four Na-ions are inserted during sodiation, only 1.95 Na^+ can be extracted during the first desodiation.

Operando imaging techniques are extremely useful for analysis of transformations in alloying anodes. Wang *et al.* [7] used *operando* full-field TXM tomography to image Sn particles in an alloying NIB anode in 3D during cycling. Larger particles were observed to expand and crack during sodiation, leading to poor cycling life, while particles smaller than 0.5 µm are less prone to cracking and can be cycled for longer (Figure 10).

10.1002/batt.202000294

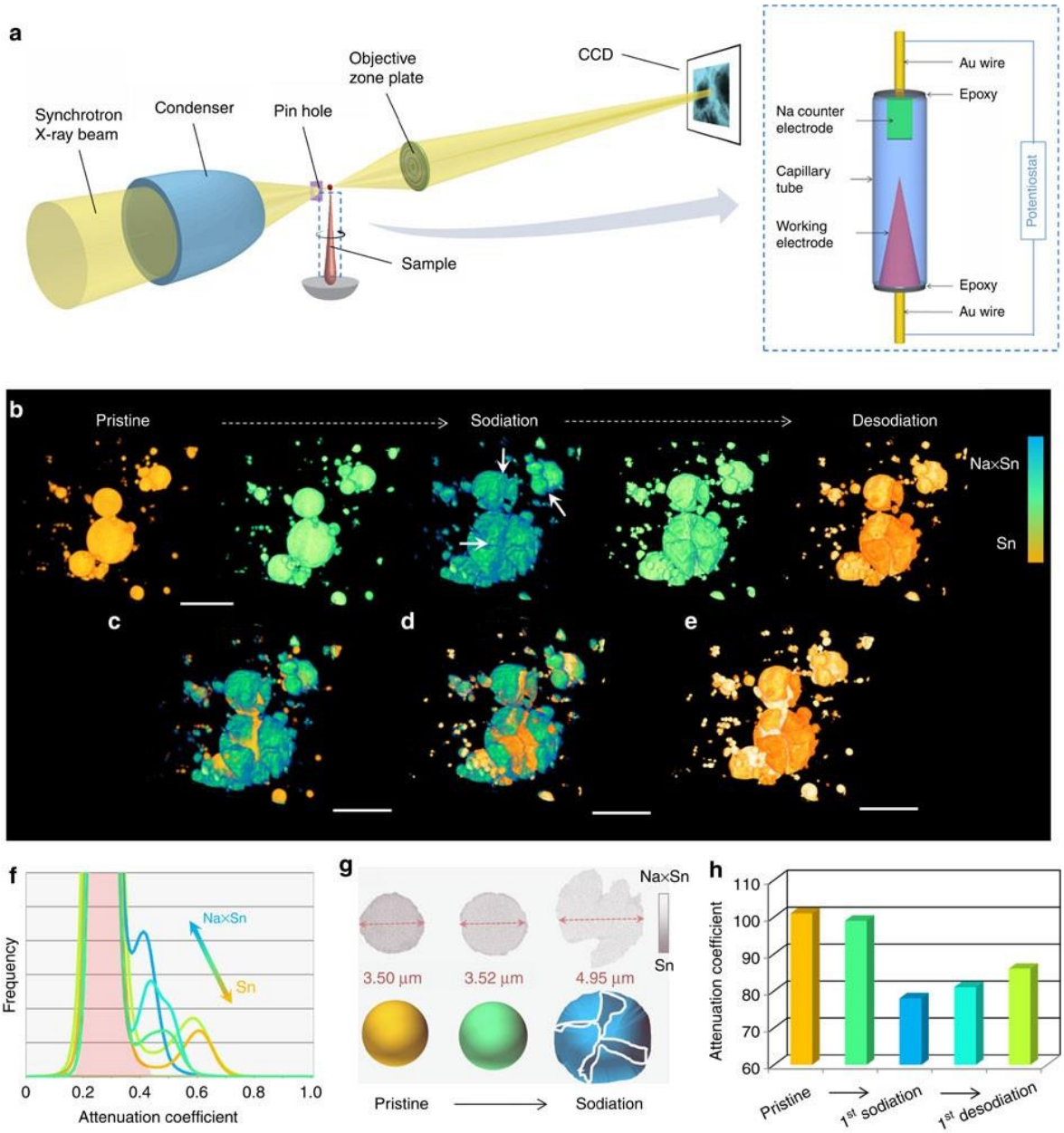

Figure 10: (a) Experimental setup and electrochemical cells for operando TXM. (b) 3D morphological change of Sn particles during the first sodiation and desodiation. The colours represent the attenuation coefficient variation, shown in (h), within the reconstructed images. Overlapped 3D images of Sn particles at different cyclingstages: (c) pristine/sodiated, (d) sodiated/desodiated and (e) pristine/desodiated. The contrasts of the overlapping colours (c–e) are adjusted for better visualization. (f) Normalized X-ray attenuation coefficient graph during the first cycle. (g) Schematic illustration showing the volume expansion and cracking during the sodiation process supported by the cross-section images of selected particles (shown in grey). (h) Histogram of attenuation coefficient change, correlated to the 3D morphological and chemical changes. Scale bar: 10 µm. Reprinted (adapted) with permission from [7].

Lim *et al.* [41] combined TXM with XRD to analyse a Bi electrode during sodiation. A core-shell pattern (similar to that of the materials described above) is observed, accompanied by a sudden volume change, which leads to cracking. The particles do not shrink significantly on desodiation, leaving behind a porous microstructure.

Sottmann *et al.* [40] were the first to use *operando* XRD/PDF computed tomography (XRD/PDF-CT) to study specific NIB components, separating the contributions of the different components (e.g., electrodes, current collectors, electrolyte, and binders). This provided PDF data of very

high-quality for mechanistic studies on the anode (see section 2.4 above) and allowed mapping of the structural variations in the crystalline Na_3P using Rietveld analysis.

5. Experimental setup, *operando* cells

Operando measurements on batteries require specially designed electrochemical cells and setups that are adapted to the inherent constraints of the instrument used for measurements (within the present review: X-ray diffraction/scattering, absorption and imaging) [20-23]. These X-ray transparent electrochemical cells should ideally mimic the configuration of real batteries in terms of pressure on the stack of battery components, volume of electrolyte with respect to electrode material and thickness of the working electrode. Thus, many of the reported cells are modifications of standard electrochemical cells used in the research laboratory (coin, pouch and Swagelok cells). For meaningful *operando* characterization, the cell should reproduce a typical electrochemical operation of a common electrochemical test cell. Air and moisture sensitive battery components need to be hermetically sealed in inert atmosphere and shielded from air. The container and window materials should further be chemically inert with respect to the other battery components. The *operando* cell should also be designed for easy assembly/disassembly. The cell design for the *operando* X-ray diffraction/scattering, absorption and imaging mainly varies in the orientation of the stack of battery components with respect to the X-ray beam, the type of X-ray transparent window/container materials that can be used and the dimensions of the electrodes.

X-ray diffraction/scattering and XAS measurements are commonly performed perpendicular to the plane of the electrode layers; this geometry only allows one to observe changes in the working electrode if signals from other cell components can be removed, masked or ignored. The stack of battery components is typically pressed together by parts containing X-ray transparent windows [21, 189]. The cell designs can be separated into disposable (coin [190] or pouch cell [191, 192]) and reusable (Swagelok-type [189, 193-196]). For some of these cells automated sample changers are available, which permits more efficient use of experimental time [189-191, 193]. For the disposable cells, Kapton (polyimide) film or Parafilm can be used as X-ray windows, Figure 11a [190, 192]. However, depending on the film thickness, their flexibility can reduce the homogeneity of pressure across electrode layer, with corresponding variations in chemistry [197-199]. These issues can be avoided in the reusable Swagelok-type cells, where besides Kapton [189, 195] and aluminum foils [196] also, more costly but rigid and electrically conducting window materials such as glassy carbon [193] or beryllium (Be) [194] can be used, as shown in Figure 11b and 11c. Readers should note that Be and its compounds are highly toxic, so must be handled with extreme care. Another disadvantage of Be windows is their Bragg peaks, which could overlap with those of active material. Aluminum foil (often placed between the Be window and positive electrode materials to prevent oxidation of Be) [194] also introduces diffraction peaks. Glassy carbon is amorphous, resulting in a broad background contribution (no Bragg peaks) and non-hazardous. Beryllium is less absorbing than glassy carbon.

For XAS, particularly in the energy range of transition metal K-edges, Be and Kapton are the preferred window materials due to their higher transmission. In some cases, holes are punched through the current collectors, counter electrode and separator. The volume of electrolyte can also be reduced, to further improve beam transmission [200]. With these optimizations, XAS spectra of most transition metals and alloying elements can be obtained in transmission geometry. For the lighter elements and/or small concentrations, however, fluorescence mode (reflection geometry) is preferable.

Higher energies are typically used for diffraction/scattering experiments, compared to XAS, (at the synchrotron or with e.g. Mo radiation on laboratory diffractometers) [189] so transmission through the cell (Debye–Scherrer geometry) is usually not a problem. It is then possible to collect scattering data from both electrodes in a full-cell simultaneously. Some cells use a reflection configuration (Bragg–Brentano geometry), which is commonly available in laboratory X-ray diffractometers with Cu radiation. In such experiments, a surface layer with an angle- and composition-dependent depth is sampled instead of the entire depth of the working electrode as in transmission geometry. The available cell designs include a reusable Swagelok-type cell with a beryllium window [201], a reusable cell with glassy carbon windows [202], a reusable cell with a graphite dome as the window [109], a disposable coin cell with a Kapton window [203] and a pouch cell with an Al/Ti metal foil window [192]. The similarities between the cell designs for X-ray diffraction/scattering and absorption make parallel XRD and XAS experiments possible on some beamlines. This enables deep insights into electrochemical processes by both structural and chemical characterization of the electrode material(s) *quasi*-simultaneously (at the same voltage or state of charge) in the same cell [189, 204].

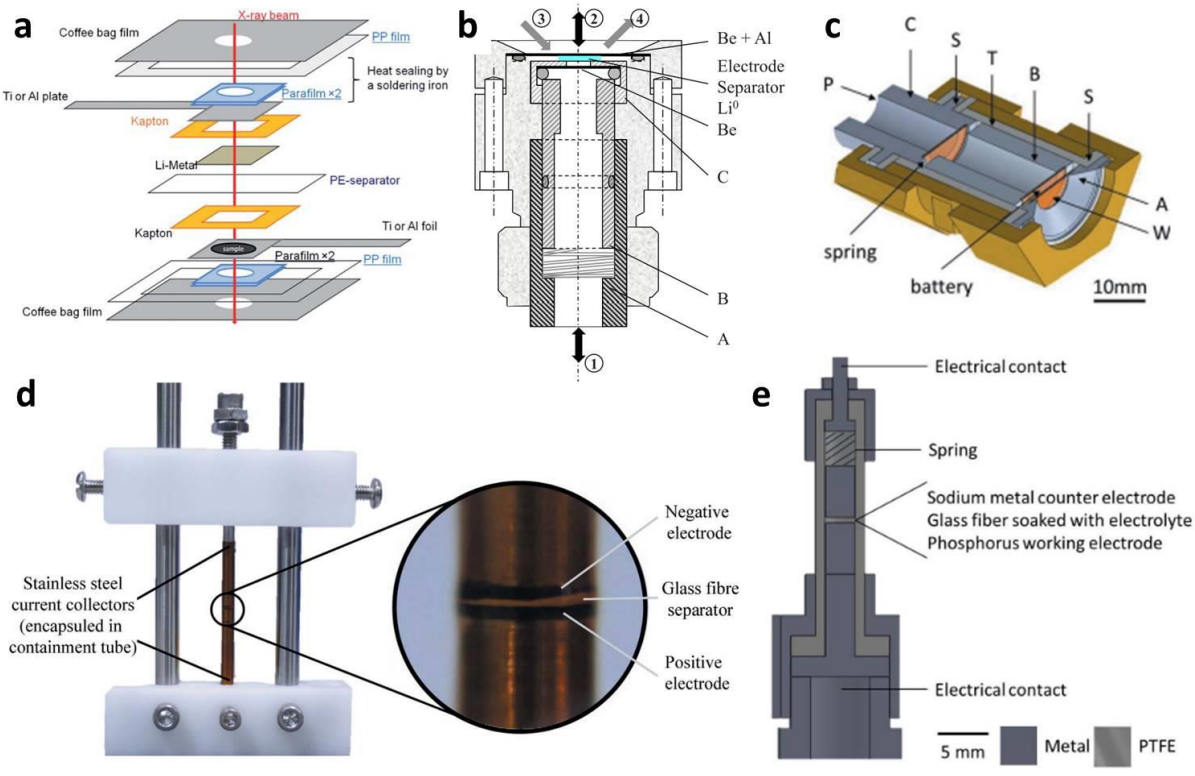

Figure 11: Illustration of operando cell designs based on (a) pouch cells [192], Swagelok-type cell with (b) Be window [194] and (c) Kapton [189], 3D imaging cells with (d) alignment rods [205] and (e) PTFE casing [206].

X-ray imaging is performed in full-field or scanning modes. Each cell design was modified to minimize adsorption of hard X-rays, allowing an unobstructed view of the region of interest (e.g. a few electrode particles, a slice of the electrode or the entire stack of battery components) [22, 23]. For three-dimensional (3D) imaging rotation of the object (ideally at least 180°) is required. The rotation axis is typically chosen perpendicular to the stack of components and the X-ray beam is oriented in the plane of the electrode layer(s). *Operando* cells for 3D imaging typically, therefore, have a cylindrical shape. The container walls are made of thin, mechanically stable, electrochemically inert, electrically insulating, X-ray transparent and texture-free materials, e.g. Kapton, quartz glass, PEEK and PTFE. The diameter of the cell has

to be sufficiently small to reduce absorption of the X-rays in the selected energy range by electrode materials and electrolyte. Smaller versions can be built from quartz glass capillaries (~1 mm in diameter). The electrodes are fixed to metal wires glued into the capillary with epoxy, which also hermetically seals the cell. Planar cells, e.g. pouch cells [207], and cylindrical cells with alignment rods (Figure 11d-e) [205], can be used for tomographic imaging with less than 180° rotation. However, the missing angular wedge may cause artefacts, some of which can be removed with sophisticated reconstruction algorithms [208].

6. Methods for analysis of *operando* data/new-experimental methodologies

Fitting the large volumes of data produced by modern *operando* experiments is a significant task. Modern computing and software make this process significantly easier, and several methods developed recently are extremely applicable for *operando* NIB studies. At the time of writing, few of these methods have been applied to NIBs. Therefore, this section will cast its net wider in terms of chemistries studied than the bulk of the review.

Batch fitting methods have been used since the early days of *in situ* and *operando* studies, for example, fitting of Bragg peak intensities to obtain crystallisation kinetics during zeolite structure transformations [209]. In a batch (or sequential) pattern fitting process, the initial structural model is refined against the starting dataset and the refined model is taken as the starting point for refinement against the next dataset in the series. In this way, the model "evolves" through the process as it is refined against each dataset. This method has been applied to diffraction, scattering and spectroscopic data series [210, 211]. Some Rietveld and PDF refinement software packages, e.g. Fullprof [212, 213] and PDFGUI include specific tools for batch refinement, or function with software designed by others to facilitate it [214]. Batch refinement was used by Gaubicher *et al.* in an early *operando* study on NIBs [139]. Batch processing is also part of the popular ATHENA [215] suite for XAS data processing, used in the first *operando* XAS study of NIBs [216].

The surface/parametric approach to pattern fitting developed by Stinton and Evans [217] has been applied in several *operando* studies of NIB materials [42, 206, 216-220]. In this method, the entire series of diffraction patterns or spectra are treated simultaneously. Parameters like the instrumental peak shape and diffractometer zero point can be refined globally against all the data, while parameters that can vary during the experiment are refined separately for each diffraction pattern/spectrum. The approach is especially useful for *operando* diffraction computed tomography studies [221], which produce massive volumes of data, as the number of refined parameters can be significantly reduced compared to batch methods. An example is the XRD-CT mapping presented by Sottmann *et al.* on a working phosphorus NIB anode [206]. Linking less interesting, well understood parameters to equations which describe their physical behaviour can further improve the stability and precision of parametric fits [222]. An intriguing extension of this approach is the direct least-squares reconstruction (DLSR) method for XRD-CT recently described by Vamvakeros *et al.* [223]. Here, the reconstruction and Rietveld refinement are carried out simultaneously using a parametric approach in which the groups of measured diffraction patterns merged to reconstruct each voxel, are refined simultaneously against a single physical model for the relevant voxel. DLSR allows reconstruction of larger objects without blurring at the periphery of the tomograms caused by parallax artefacts. This

has obvious benefits for electrochemistry, as the use of larger, more realistic cells reduces inaccuracies in e.g. calculated capacity from electrode mass, as larger masses are easier to measure accurately, not to mention being easier to handle.

The use of structures from density functional theory (DFT) calculations (energy minimisations both of known structures from databases and invented structures produced, e.g. by replacement of certain atom types in a known structure) has already proved important in interpreting operando data from NIBs [42, 43, 171, 206, 218, 224-226]. We expect such methods to find new applications as *operando* experiments develop further and come into wider use. The development of databases of computed properties like Materials Project [227] and machine learning approaches to prediction of materials with desirable properties will also accelerate this process.

Principle component analysis (PCA) is a statistical multivariate curve resolution (MCR) method that has been used for several decades to analyse spectroscopic data [228] and has more recently been applied to diffraction [229, 230] and PDF [231]. PCA takes a dataset with many variables and extracts a small number of new variables that express the bulk of the variance [232]. In *operando* battery cycling studies, where we expect to see variations in the structure and composition of the active components during the experiment, PCA can extract the signals responsible for most of the variance in the data series without any prior knowledge of the chemistry. These principal components should represent the signals of the active components that change during the experiment.

PCA is a very powerful tool for rapidly determining the key sources variance in a series of many spectra/patterns. An interesting recent example is the use of *in situ* XRD/PDF/fiber optic reflectance spectroscopy in an attempt to determine the lost recipe of the ancient pigment Mayan blue [233]. PCA has also been used for automatic extraction of kinetic data from *in situ* experiments combining Raman spectroscopy and XRD [234], and for efficient analysis of a large series of *in situ* single crystal datasets collected during the adsorption of CO_2 on zeolite-Y [235]. The team behind many of these developments has produced a software package, RootProf [236], for PCA analysis of diffraction and spectroscopy data.

In multivariate curve resolution with alternating least squares (MCR-ALS) [172, 237, 238], a set of factors describing the data, obtained from an MCR method like PCA, singular-value decomposition [239] or cluster analysis [240] is fitted to the data using a constrained least squares refinement [241]. The power of this approach lies in the possibility of inserting constraints obtained from other measurements on the same sample, allowing the combination of data from a range of sources and techniques. Application of this method to large *operando* battery XAS datasets suggests it may prove very useful in the future [172, 237, 238]. Recently, Rekhinta et al used MCR-ALS to extract and study the variable components of a PDF data series collected during the decomposition of magnesium hydroxycarbonate. They revealed, with no prior information, the existence of an amorphous intermediate phase in the process that was not evident from other examinations of the experimental PDFs. Although PCA and MCR-ALS are yet to be applied to *operando* battery PDF data, we believe that they will prove very useful in future for extracting signals from weakly scattering but highly variable amorphous components that appear during cycling.

Modulation excitation is another technique that makes a virtue of the huge number of data points obtained from an *operando* experiment. In this case, there is an experimental element as well as statistical analysis. A series of structural data (spectra, diffraction patterns, etc.) are collected from a sample while a modulated external stimulus is applied. This could be anything from a switchable electric field to a changing series of reactive gases [242]. The variations in the structural data are then plotted against the frequency of modulation of the stimulus. When the series of data is processed correctly against the modulation frequency, signals which do not vary with the external stimulus collapse to zero intensity, leaving only the signals from parts of the sample that vary along with it. This can significantly simplify the data by wiping out the contribution of spectator species that might otherwise have a strong contribution to the spectra/patterns. The approach was first applied to spectroscopy by Urakawa and co-workers [243] and subsequently developed for diffraction data [244], but has not thus far been applied to a large range of systems. The potential for processing *operando* data on battery cycling with this method is obvious, as a modulated stimulus is already an integral part of the experiment. Chernyshov *et al.* recently compared the use of PCA and modulation excitation analysis for synchrotron diffraction data on gas loading of the porous framework gamma $Mg(BH_4)_2$ [245].

The potential of machine learning (ML) and artificial intelligence (AI) methods for spotting trends in massive datasets, which might be ignored by careless humans, is immense but is currently untapped in the field of *operando* NIB studies. An indication of the possibilities comes from the use of machine learning to carry out an extensive statistical analysis of tomographic data on the detachment of NMC particles in an LIB cathode from their conductive carbon support [246].

7. Main challenges and future perspective

In the ongoing search for alternatives to LIBs, NIBs (and potentially Na-air and Na-S batteries) offer promise for several applications. However, NIBs still lack the performance required to be truly competitive with LIBs. Therefore, the search for more efficient, stable, cheap and environmentally friendly materials continues. The rational design of NIB materials requires a deep understanding of their behaviour in electrochemical systems that are as close as possible to real applications. *Operando* X-ray methodologies deliver valuable information about the structural, atomistic and morphological changes while the battery is actually in its working state. In some cases, data can be obtained with spatial resolution. Although X-ray methods have limitations (limited resolution, beam damage, lack of surface sensitivity) several of which are accentuated when they are used for *operando* characterization, the methods described above are suitable for a wide range of both crystalline and amorphous materials. In particular, beam damage remains a bottleneck in the *in situ* and *operando* characterizations, not only for NIBs but also for all kind of battery systems [25, 247, 248].

Crystalline TMO cathodes, in particular, are perfect samples for both XRD and XAS methods. Furthermore, PDF has proved to be an extremely powerful technique for analysis of conversion and alloying anode materials, which often become amorphous during cycling. One practical problem specific to *operando* XRD/PDF measurements on NIB half-cells with Na metal counter electrodes is the very strong scattering from the Na foil. This signal can have very strong preferred orientation effects (sometimes giving single crystal-like diffraction spots), which move during the experiment due to expansion and contraction of the active material(s).

This problem is most commonly addressed by masking out the areas of the diffraction pattern where the Na peaks are observed, however, this can lead to the loss of valuable sample information. We expect that in the near future *operando* XRD/PDF CT methods will increase in popularity as they provide an extraordinary amount of information for understanding NIB performance. These methods also directly target the components of interest, removing the contributions from electrolyte, current collectors, sodium metal half-cell electrodes etc. MCR methods like PCA and modulation enhanced diffraction/spectroscopy also offer the promise of extracting signals for the active materials while excluding the Na metal signal. An obvious experimental solution to problems with Na metal counter electrodes, is, of course, to use full cells for *operando* studies. This, however, adds another significant and variant contribution to the data.

A broad range of *operando* X-ray methods can now be applied both at synchrotrons and in the home laboratory, and many electrochemical cell designs are available. These offer tremendous scope for new *operando* investigations of working and degradation mechanisms in NIBs. Analysis of the sometimes extremely large datasets generated during these measurements (e.g. XRD-CT) will continue to become easier as advanced analysis tools develop and gain wider acceptance. A significant gap in the sensitivity of *operando* battery methods remains the detection of thin layers and coatings, both those formed during cycling and those applied to battery components to improve their properties. We expect that ongoing improvements in X-ray brilliance and focussing of smaller beams at synchrotron sources, along with new sample cell developments will address this in the next few years.

While X-ray based methods are well established for *operando* characterization of battery materials, the *operando* application of other, complementary methods will allow even more complete characterisation of these complex systems. In the near future we expect to see the use of techniques combining X-ray methods with TEM, AFM and Raman for *operando* NIB studies. In combination, this suite of *operando* methods will provide very complete descriptions of NIBs.

Further optimization and development of the new materials and chemistries will require understanding not only of bulk processes, but also of the interfaces between various materials and components. Thus, we expect the rise of surface *operando* techniques such as Raman and FTIR spectroscopies as well as X-ray surface methods in the near future. *Operando* HAXPES [249] (Hard X-ray Photoelectron Spectroscopy) has already been used for LIBs and synchrotron-based SOXPES (Soft X-ray Photoelectron Spectroscopy) [250] applied in the study of SEI formation in NIBs, but only *in situ*.

Operando methods deliver chemical and structural information of such high value that a growing number of researchers consider them worthwhile, despite the complexity of the experimental setups and data processing. Considering the importance of battery science, we predict further expansion of their use, providing the basis for further materials and technology development.

Acknowledgments

The authors thank the Research Council of Norway (NFR) for funding through the NanoName project (number 287480). This work was performed within MoZEES, a Norwegian Centre for Environment-friendly Energy Research (FME), co-sponsored by the Research Council of Norway (project number 257653) and 40 partners from research, industry and public sector.

DSW thanks Antony Vamvakeros, Wouter Van Beek and Dmitri Chernyshov for discussions on DLSR, modulation excitation and PCA methods. CC would like to thank Dr Muhammad Abdelhamid for helping with the graphics.

Author Contributions

Anders Brennhagen: Writing - review & editing, Methodology, Formal analysis, Visualization. Carmen Cavallo: Writing - review & editing, Supervision, Visualization. David Wragg: Writing - review & editing, Visualization. Jonas Sottmann: Writing - review & editing, Visualization. Alexey Koposov: Writing - review & editing, Visualization. Helmer Fjellvåg: Review & editing.

Table of Contents

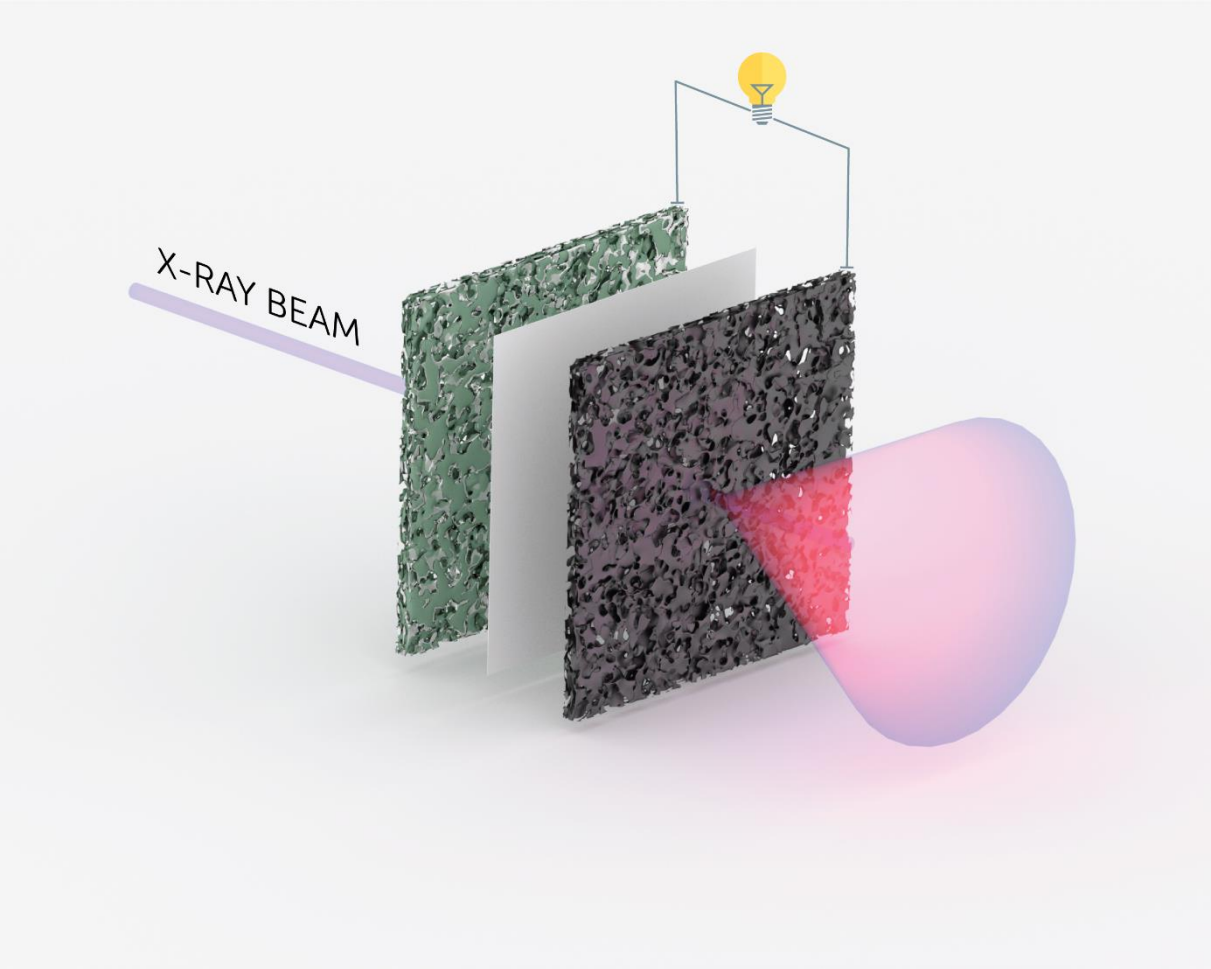

Operando studies provide extremely valuable insights for understanding (de)sodiation mechanisms during electrochemical cycling. We offer a critical summary of the *operando* X-ray based characterization techniques that have been applied to Na-ion, Na-air and Na-sulfur batteries. The review also covers cell design, data processing and future opportunities to give a 360°C overview of *operando* X-ray-based techniques in Na battery applications.

Keywords

Operando X-ray Methods, Sodiation and desodiation mechanism, Cell design, Data analysis for *Operando*, Sodium batteries.

References

[1] I. Hasa, S. Mariyappan, D. Saurel, P. Adelhelm, A. Y. Koposov, C. Masquelier, L. Croguennec, M. Casas-Cabanas, *J. Power Sources* **2021**, *482*, 228872.
[2] C. Vaalma, D. Buchholz, M. Weil, S. Passerini, *Nat. Rev. Mater.* **2018**, *3*, 18013.
[3] M. I. Jamesh, A. S. Prakash, *J. Power Sources* **2018**, *378*, 268-300.
[4] X. Yin, S. Sarkar, S. Shi, Q.-A. Huang, H. Zhao, L. Yan, Y. Zhao, J. Zhang, *Adv. Funct. Mater.* **2020**, *30*, 1908445.
[5] K. Nobuhara, H. Nakayama, M. Nose, S. Nakanishi, H. Iba, *J. Power Sources* **2013**, *243*, 585-587.
[6] Z. Wang, S. M. Selbach, T. Grande, *RSC Adv.* **2014**, *4*, 4069-4079.
[7] J. Wang, C. Eng, Y.-c. K. Chen-Wiegart, J. Wang, *Nat. Commun.* **2015**, *6*, 1-9.
[8] W. Brehm, A. L. Santhosha, Z. Zhang, C. Neumann, A. Turchanin, A. Martin, N. Pinna, M. Seyring, M. Rettenmayr, J. R. Buchheim, P. Adelhelm, *Adv. Funct. Mater.* **2020**, *30*, 1910583.
[9] H. Li, K. Qian, X. Qin, D. Liu, R. Shi, A. Ran, C. Han, Y.-B. He, F. Kang, B. Li, *J. Power Sources* **2018**, *385*, 114-121.
[10] E. de la Llave, V. Borgel, K.-J. Park, J.-Y. Hwang, Y.-K. Sun, P. Hartmann, F.-F. Chesneau, D. Aurbach, *ACS Appl. Mater. Interfaces* **2016**, *8*, 1867-1875.
[11] Y. Lu, Q. Zhang, J. Chen, *Sci. China: Chem.* **2019**, *62*, 533-548.
[12] X. Pu, H. Wang, D. Zhao, H. Yang, X. Ai, S. Cao, Z. Chen, Y. Cao, *Small* **2019**, *15*, 1805427.
[13] W. Zhu, Y. Wang, D. Liu, V. Gariépy, C. Gagnon, A. Vijh, M. L. Trudeau, K. Zaghib, *Energies* **2018**, *11*, 2963.
[14] D. Liu, Z. Shadike, R. Lin, K. Qian, H. Li, K. Li, S. Wang, Q. Yu, M. Liu, S. Ganapathy, *Adv. Mater.* **2019**, *31*, 1806620.
[15] G. Zhang, T. Xiong, L. He, M. Yan, K. Zhao, X. Xu, L. Mai, *J. Mater. Sci.* **2017**, *52*, 3697-3718.
[16] S. Mukherjee, S. Bin Mujib, D. Soares, G. Singh, *Materials* **2019**, *12*, 1952.
[17] A. M. Tripathi, W.-N. Su, B. J. Hwang, *Chem. Soc. Rev.* **2018**, *47*, 736-851.
[18] J. Li, C. Arbizzani, S. Kjelstrup, J. Xiao, Y.-y. Xia, Y. Yu, Y. Yang, I. Belharouak, T. Zawodzinski, S.-T. Myung, *J. Power Sources* **2020**, *452*, 227824.
[19] H. Gao, W. Ma, W. Yang, J. Wang, J. Niu, F. Luo, Z. Peng, Z. Zhang, *J. Power Sources* **2018**, *379*, 1-9.
[20] S.-M. Bak, Z. Shadike, R. Lin, X. Yu, X.-Q. Yang, *NPG Asia Mater.* **2018**, *10*, 563-580.
[21] R. D. Marco, J.-P. Veder, *TrAC, Trends Anal. Chem.* **2010**, *29*, 528-537.
[22] L. Wang, J. Wang, P. Zuo, *Small Methods* **2018**, *2*, 1700293.
[23] J. Nelson Weker, M. F. Toney, *Adv. Funct. Mater.* **2015**, *25*, 1622-1637.
[24] P. Harks, F. Mulder, P. Notten, *J. Power Sources* **2015**, *288*, 92-105.
[25] J. Conder, C. Marino, P. Novák, C. Villevieille, *J. Mater. Chem. A* **2018**, *6*, 3304-3327.
[26] R. R. Chianelli, *J. Electrochem. Soc.* **1978**, *125*, 1563.
[27] M. S. Whittingham, *Science* **1976**, *192*, 1126-1127.
[28] B. M. Weckhuysen, *Phys. Chem. Chem. Phys.* **2003**, *5*, 4351-4360.
[29] M. A. Bañares, M. O. Guerrero-Pérez, J. L. G. Fierro, G. G. Cortez, *J. Mater. Chem.* **2002**, *12*, 3337-3342.
[30] M. Banares, I. Wachs, *J. Raman Spectrosc.* **2002**, *33*, 359-380.
[31] M. Guerrero-Pérez, M. Banares, *Chem. Commun.* **2002**, *12*, 1292-1293.
[32] C. Giacovazzo, H. L. Monaco, D. Viterbo, F. Scordari, G. Gilli, G. Zanotti, M. Catti, *Fundamentals of crystallography, Vol. 7*, Oxford University Press Oxford, **2002**.
[33] C. Suryanarayana, M. G. Norton, *X-Ray Diffraction*, Springer, **1998**.
[34] T. Egami, S. J. Billinge, *Underneath the Bragg peaks: structural analysis of complex materials*, Newnes, **2012**.
[35] H. Gao, X. Yan, J. Niu, Y. Zhang, M. Song, Y. Shi, W. Ma, J. Qin, Z. Zhang, *Chem. Eng. J.* **2020**, *388*, 124299.

[36] M. Povia, J. Sottmann, G. Portale, K. D. Knudsen, S. Margadonna, S. Sartori, *J. Phys. Chem. C* **2018**, *122*, 5917-5923.
[37] H. Gao, J. Niu, C. Zhang, Z. Peng, Z. Zhang, *ACS Nano* **2018**, *12*, 3568-3577.
[38] M. Arnaiz, J. L. Gómez-Cámer, J. Ajuria, F. Bonilla, B. Acebedo, M. Jáuregui, E. Goikolea, M. Galceran, T. Rojo, *Chem. Mater.* **2018**, *30*, 8155-8163.
[39] L. Zhang, X. Hu, C. Chen, H. Guo, X. Liu, G. Xu, H. Zhong, S. Cheng, P. Wu, J. Meng, *Adv. Mater.* **2017**, *29*, 1604708.
[40] J. Sottmann, M. Di Michiel, H. Fjellvåg, L. Malavasi, S. Margadonna, P. Vajeeston, G. B. Vaughan, D. S. Wragg, *Angew. Chem., Int. Ed.* **2017**, *56*, 11385-11389.
[41] C.-H. Lim, B. Selvaraj, Y.-F. Song, C.-C. Wang, J.-T. Jin, S.-S. Huang, C.-H. Chuang, H.-S. Sheu, Y.-F. Liao, N.-L. Wu, *J. Mater. Chem. A* **2017**, *5*, 21536-21541.
[42] J. Sottmann, M. Herrmann, P. Vajeeston, Y. Hu, A. Ruud, C. Drathen, H. Emerich, H. Fjellvåg, D. S. Wragg, *Chem. Mater.* **2016**, *28*, 2750-2756.
[43] P. K. Allan, J. M. Griffin, A. Darwiche, O. J. Borkiewicz, K. M. Wiaderek, K. W. Chapman, A. J. Morris, P. J. Chupas, L. Monconduit, C. P. Grey, *J. Am. Chem. Soc.* **2016**, *138*, 2352-2365.
[44] J. K. Mathiesen, R. Väli, M. Härmas, E. Lust, J. Fold von Bülow, K. M. Ø. Jensen, P. Norby, *J. Mater. Chem. A* **2019**, *7*, 11709-11717.
[45] A. Beda, C. Villevieille, P.-L. Taberna, P. Simon, C. M. Ghimbeu, *J. Mater. Chem. A* **2020**, *8*, 5558-5571.
[46] H.-J. Liang, B.-H. Hou, W.-H. Li, Q.-L. Ning, X. Yang, Z.-Y. Gu, X.-J. Nie, G. Wang, X.-L. Wu, *Energy Environ. Sci.* **2019**, *12*, 3575-3584.
[47] L. Seidl, N. Bucher, E. Chu, S. Hartung, S. Martens, O. Schneider, U. Stimming, *Energy Environ. Sci.* **2017**, *10*, 1631-1642.
[48] T. Yang, X. Niu, T. Qian, X. Shen, J. Zhou, N. Xu, C. Yan, *Nanoscale* **2016**, *8*, 15497-15504.
[49] H. Kim, J. Hong, G. Yoon, H. Kim, K.-Y. Park, M.-S. Park, W.-S. Yoon, K. Kang, *Energy Environ. Sci.* **2015**, *8*, 2963-2969.
[50] Y. Lee, C.-H. Jo, J.-K. Yoo, J. U. Choi, W. Ko, H. Park, J. H. Jo, D. O. Shin, S.-T. Myung, J. Kim, *Energy Storage Materials* **2020**, *24*, 458-466.
[51] X.-M. Lin, J.-H. Chen, J.-J. Fan, Y. Ma, P. Radjenovic, Q.-C. Xu, L. Huang, S. Passerini, Z.-Q. Tian, J.-F. Li, *Adv. Energy Mater.* **2019**, *9*, 1902312.
[52] Z. Chen, X. Cheng, H. Yu, H. Zhu, R. Zheng, T. Liu, J. Zhang, M. Shui, J. Shu, *Ceram. Int.* **2018**, *44*, 17094-17101.
[53] C. Dong, J. Liang, Y. He, C. Li, X. Chen, L. Guo, F. Tian, Y. Qian, L. Xu, *ACS Nano* **2018**, *12*, 8277-8287.
[54] L. Wang, J. Wang, F. Guo, L. Ma, Y. Ren, T. Wu, P. Zuo, G. Yin, J. Wang, *Nano Energy* **2018**, *43*, 184-191.
[55] G.-L. Xu, T. Sheng, L. Chong, T. Ma, C.-J. Sun, X. Zuo, D.-J. Liu, Y. Ren, X. Zhang, Y. Liu, *Nano letters* **2017**, *17*, 953-962.
[56] X. Ou, X. Liang, F. Zheng, P. Wu, Q. Pan, X. Xiong, C. Yang, M. Liu, *Electrochim. Acta* **2017**, *258*, 1387-1396.
[57] X. Ou, J. Li, F. Zheng, P. Wu, Q. Pan, X. Xiong, C. Yang, M. Liu, *J. Power Sources* **2017**, *343*, 483-491.
[58] Z. Huang, H. Hou, C. Wang, S. Li, Y. Zhang, X. Ji, *Chem. Mater.* **2017**, *29*, 7313-7322.
[59] P. Bleith, H. Kaiser, P. Novák, C. Villevieille, *Electrochim. Acta* **2015**, *176*, 18-21.
[60] J. Fullenwarth, A. Darwiche, A. Soares, B. Donnadieu, L. Monconduit, *J. Mater. Chem. A* **2014**, *2*, 2050-2059.
[61] E. Edison, P. K. Gogoi, Y. Zheng, S. Sreejith, S. J. Pennycook, C. T. Lim, M. Srinivasan, *ACS Appl. Mater. Interfaces* **2019**, *11*, 20082-20090.
[62] X. Shi, S.-L. Chen, H.-N. Fan, X.-H. Chen, D. Yuan, Q. Tang, A. Hu, W.-B. Luo, H.-K. Liu, *ChemSusChem* **2019**, *12*, 4046-4053.
[63] X. Ou, C. Yang, X. Xiong, F. Zheng, Q. Pan, C. Jin, M. Liu, K. Huang, *Adv. Funct. Mater.* **2017**, *27*, 1606242.

[64] J. Sottmann, R. Homs-Regojo, D. S. Wragg, H. Fjellvåg, S. Margadonna, H. Emerich, *J. Appl. Crystallogr.* **2016**, *49*, 1972-1981.
[65] A. Darwiche, M. Toiron, M. T. Sougrati, B. Fraisse, L. Stievano, L. Monconduit, *J. Power Sources* **2015**, *280*, 588-592.
[66] L. Baggetto, H.-Y. Hah, C. E. Johnson, C. A. Bridges, J. A. Johnson, G. M. Veith, *Phys. Chem. Chem. Phys.* **2014**, *16*, 9538-9545.
[67] K. Liu, S. Tan, J. Moon, C. J. Jafta, C. Li, T. Kobayashi, H. Lyu, C. A. Bridges, S. Men, W. Guo, *Adv. Energy Mater.* **2020**.
[68] X. Cao, H. Li, Y. Qiao, X. Li, M. Jia, J. Cabana, H. Zhou, *Adv. Energy Mater.* **2020**, 1903785.
[69] E. Marelli, C. Marino, C. Bolli, C. Villevieille, *J. Power Sources* **2019**, *450*, 227617.
[70] F. Ding, C. Zhao, D. Zhou, Q. Meng, D. Xiao, Q. Zhang, Y. Niu, Y. Li, X. Rong, Y. Lu, L. Chen, Y.-S. Hu, *Energy Storage Materials* **2020**, *30*, 420-430.
[71] A. Kulka, C. Marino, K. Walczak, C. Borca, C. Bolli, P. Novák, C. Villevieille, *J. Mater. Chem. A* **2020**, *8*, 6022-6033.
[72] C. Heubner, B. Matthey, T. Lein, F. Wolke, T. Liebmann, C. Lämmel, M. Schneider, M. Herrmann, A. Michaelis, *Energy Storage Materials* **2020**, *27*, 377-386.
[73] Y. Zhu, W. Nie, P. Chen, Y. Zhou, Y. Xu, *Int. J. Energy Res.* **2020**, *44*, 3253-3259.
[74] Y. Yu, W. Kong, Q. Li, D. Ning, G. Schuck, G. Schumacher, C. Su, X. Liu, *ACS Appl. Energy Mater.* **2020**, *3*, 933-942.
[75] D. Goonetilleke, S. Wang, E. Gonzalo, M. Galcerán, D. Saurel, S. J. Day, F. Fauth, T. Rojo, N. Sharma, *J. Mater. Chem. A* **2019**, *7*, 12115-12125.
[76] A. J. Perez, G. l. Rousse, J.-M. Tarascon, *Inorg. Chem.* **2019**, *58*, 15644-15651.
[77] J. W. Somerville, A. Sobkowiak, N. Tapia-Ruiz, J. Billaud, J. G. Lozano, R. A. House, L. C. Gallington, T. Ericsson, L. Häggström, M. R. Roberts, *Energy Environ. Sci.* **2019**, *12*, 2223-2232.
[78] Y. Xiao, Y.-F. Zhu, H.-R. Yao, P.-F. Wang, X.-D. Zhang, H. Li, X. Yang, L. Gu, Y.-C. Li, T. Wang, Y.-X. Yin, X.-D. Guo, B.-H. Zhong, Y.-G. Guo, *Adv. Energy Mater.* **2019**, *9*, 1803978.
[79] D. Sehrawat, S. Cheong, A. Rawal, A. M. Glushenkov, H. E. A. Brand, B. Cowie, E. Gonzalo, T. Rojo, P. J. P. Naeyaert, C. D. Ling, M. Avdeev, N. Sharma, *CrystEngComm* **2019**, *21*, 172-181.
[80] Q. Liu, Z. Hu, M. Chen, C. Zou, H. Jin, S. Wang, Q. Gu, S. Chou, *J. Mater. Chem. A* **2019**, *7*, 9215-9221.
[81] Y. Wen, J. Fan, C. Shi, P. Dai, Y. Hong, R. Wang, L. Wu, Z. Zhou, J. Li, L. Huang, S.-G. Sun, *Nano Energy* **2019**, *60*, 162-170.
[82] W. Kong, H. Wang, L. Sun, C. Su, X. Liu, *Appl. Surf. Sci.* **2019**, *497*, 143814.
[83] S. Kjeldgaard, S. Birgisson, A. G. Kielland, B. B. Iversen, *J. Appl. Crystallogr.* **2018**, *51*, 1304-1310.
[84] X. Chen, S. Hwang, R. Chisnell, Y. Wang, F. Wu, S. Kim, J. W. Lynn, D. Su, X. Li, *Adv. Funct. Mater.* **2018**, *28*, 1803896.
[85] N. Su, Y. Lyu, B. Guo, *Electrochem. Commun.* **2018**, *87*, 71-75.
[86] E. Marelli, C. Villevieille, S. Park, N. Hérault, C. Marino, *ACS Appl. Energy Mater.* **2018**, *1*, 5960-5967.
[87] L. Yang, X. Li, X. Ma, S. Xiong, P. Liu, Y. Tang, S. Cheng, Y.-Y. Hu, M. Liu, H. Chen, *J. Power Sources* **2018**, *381*, 171-180.
[88] X. Zhang, K. Jiang, S. Guo, X. Mu, X. Zhang, P. He, M. Han, H. Zhou, *Chem. Commun.* **2018**, *54*, 12167-12170.
[89] Y. Xiao, P.-F. Wang, Y.-X. Yin, Y.-F. Zhu, Y.-B. Niu, X.-D. Zhang, J. Zhang, X. Yu, X.-D. Guo, B.-H. Zhong, Y.-G. Guo, *Adv. Mater.* **2018**, *30*, 1803765.
[90] L. Sun, Y. Xie, X.-Z. Liao, H. Wang, G. Tan, Z. Chen, Y. Ren, J. Gim, W. Tang, Y.-S. He, K. Amine, Z.-F. Ma, *Small* **2018**, *14*, 1704523.
[91] P. F. Wang, H. R. Yao, Y. You, Y. G. Sun, Y. X. Yin, Y. G. Guo, *Nano Res.* **2018**, *11*, 3258-3271.
[92] S. N. Lou, N. Sharma, D. Goonetilleke, W. H. Saputera, T. M. Leoni, P. Brockbank, S. Lim, D. W. Wang, J. Scott, R. Amal, *Adv. Energy Mater.* **2017**, *7*, 1700545.
[93] H. Ma, H. Su, K. Amine, X. Liu, S. Jaffer, T. Shang, L. Gu, H. Yu, *Nano Energy* **2018**, *43*, 1-10.

[94] H. Dai, C. Yang, X. Ou, X. Liang, H. Xue, W. Wang, G. Xu, *Electrochim. Acta* **2017**, *257*, 146-154.
[95] K. Kubota, Y. Yoda, S. Komaba, *J. Electrochem. Soc.* **2017**, *164*, A2368-A2373.
[96] L. Wang, J. Wang, X. Zhang, Y. Ren, P. Zuo, G. Yin, J. Wang, *Nano Energy* **2017**, *34*, 215-223.
[97] H.-R. Yao, P.-F. Wang, Y. Gong, J. Zhang, X. Yu, L. Gu, C. OuYang, Y.-X. Yin, E. Hu, X.-Q. Yang, E. Stavitski, Y.-G. Guo, L.-J. Wan, *J. Am. Chem. Soc.* **2017**, *139*, 8440-8443.
[98] P.-F. Wang, H.-R. Yao, X.-Y. Liu, J.-N. Zhang, L. Gu, X.-Q. Yu, Y.-X. Yin, Y.-G. Guo, *Adv. Mater.* **2017**, *29*, 1700210.
[99] Y. Xie, H. Wang, G. Xu, J. Wang, H. Sheng, Z. Chen, Y. Ren, C. J. Sun, J. Wen, J. Wang, *Adv. Energy Mater.* **2016**, *6*, 1601306.
[100] X. Ou, X. Xiong, F. Zheng, C. Yang, Z. Lin, R. Hu, C. Jin, Y. Chen, M. Liu, *J. Power Sources* **2016**, *325*, 410-416.
[101] K. Kubota, T. Asari, H. Yoshida, N. Yaabuuchi, H. Shiiba, M. Nakayama, S. Komaba, *Adv. Funct. Mater.* **2016**, *26*, 6047-6059.
[102] J. Wang, X. He, D. Zhou, F. Schappacher, X. Zhang, H. Liu, M. C. Stan, X. Cao, R. Kloepsch, M. S. Sofy, G. Schumacher, J. Li, *J. Mater. Chem. A* **2016**, *4*, 3431-3437.
[103] S. Hartung, N. Bucher, R. Bucher, M. Srinivasan, *Rev. Sci. Instrum.* **2015**, *86*, 086102.
[104] Y. H. Jung, A. S. Christiansen, R. E. Johnsen, P. Norby, D. K. Kim, *Adv. Funct. Mater.* **2015**, *25*, 3227-3237.
[105] B. M. de Boisse, J.-H. Cheng, D. Carlier, M. Guignard, C.-J. Pan, S. Bordere, D. Filimonov, C. Drathen, E. Suard, B.-J. Hwang, *J. Mater. Chem. A* **2015**, *3*, 10976-10989.
[106] L. Mu, S. Xu, Y. Li, Y. S. Hu, H. Li, L. Chen, X. Huang, *Adv. Mater.* **2015**, *27*, 6928-6933.
[107] N. Sharma, N. Tapia-Ruiz, G. Singh, A. R. Armstrong, J. C. Pramudita, H. E. A. Brand, J. Billaud, P. G. Bruce, T. Rojo, *Chem. Mater.* **2015**, *27*, 6976-6986.
[108] E. Talaie, V. Duffort, H. L. Smith, B. Fultz, L. F. Nazar, *Energy Environ. Sci.* **2015**, *8*, 2512-2523.
[109] Y. Shen, E. E. Pedersen, M. Christensen, B. B. Iversen, *Rev. Sci. Instrum.* **2014**, *85*, 104103.
[110] M. H. Han, E. Gonzalo, M. Casas-Cabanas, T. Rojo, *J. Power Sources* **2014**, *258*, 266-271.
[111] M. Guignard, C. Didier, J. Darriet, P. Bordet, E. Elkaïm, C. Delmas, *Nat. Mater.* **2013**, *12*, 74-80.
[112] Y.-N. Zhou, J.-J. Ding, K.-W. Nam, X. Yu, S.-M. Bak, E. Hu, J. Liu, J. Bai, H. Li, Z.-W. Fu, *J. Mater. Chem. A* **2013**, *1*, 11130-11134.
[113] Y. Xiao, Y. F. Zhu, W. Xiang, Z. G. Wu, Y. C. Li, J. Lai, S. Li, E. Wang, Z. G. Yang, C. L. Xu, B. H. Zhong, X. D. Guo, *Angew. Chem. - Int. Ed.* **2020**, *59*, 1491-1495.
[114] J. Wang, R. Gao, L. Zheng, Z. Chen, Z. Wu, L. Sun, Z. Hu, X. Liu, *ACS Catalysis* **2018**, *8*, 8953-8960.
[115] C. Liu, D. Rehnlund, W. R. Brant, J. Zhu, T. r. Gustafsson, R. Younesi, *ACS Energy Lett.* **2017**, *2*, 2440-2444.
[116] R. Pinedo, D. A. Weber, B. Bergner, D. Schröder, P. Adelhelm, J. Janek, *The J. Phys. Chem. C* **2016**, *120*, 8472-8481.
[117] Y.-X. Wang, J. Yang, W. Lai, S.-L. Chou, Q.-F. Gu, H. K. Liu, D. Zhao, S. X. Dou, *J. Am. Chem. Soc.* **2016**, *138*, 16576-16579.
[118] T. Zhu, P. Hu, C. Cai, Z. Liu, G. Hu, Q. Kuang, L. Mai, L. Zhou, *Nano Energy* **2020**, *70*, 104548.
[119] M. V. Zakharkin, O. A. Drozhzhin, S. V. Ryazantsev, D. Chernyshov, M. A. Kirsanova, I. V. Mikheev, E. M. Pazhetnov, E. V. Antipov, K. J. Stevenson, *J. Power Sources* **2020**, *470*, 228231.
[120] M. Zarrabeitia, M. a. Jáuregui, N. Sharma, J. C. Pramudita, M. Casas-Cabanas, *Chem. Mater.* **2019**, *31*, 5152-5159.
[121] F. Chen, V. M. Kovrugin, R. David, O. Mentre, F. Fauth, J. N. Chotard, C. Masquelier, *Small Methods* **2019**, *3*, 1800218.
[122] M. Galceran, J. Rikarte, M. Zarrabeitia, M. C. Pujol, M. Aguiló, M. Casas-Cabanas, *ACS Appl. Energy Mater.* **2019**, *2*, 1923-1931.
[123] L. H. B. Nguyen, J. Olchowka, S. Belin, P. Sanz Camacho, M. Duttine, A. Iadecola, F. Fauth, D. Carlier, C. Masquelier, L. Croguennec, *ACS Appl. Mater. Interfaces* **2019**, *11*, 38808-38818.

[124] D. Burova, I. Shakhova, P. Morozova, A. Iarchuk, O. A. Drozhzhin, M. G. Rozova, S. Praneetha, V. Murugan, J.-M. Tarascon, A. M. Abakumov, *RSC Adv.* **2019**, *9*, 19429-19440.
[125] M. Chen, D. Cortie, Z. Hu, H. Jin, S. Wang, Q. Gu, W. Hua, E. Wang, W. Lai, L. Chen, S.-L. Chou, X.-L. Wang, S.-X. Dou, *Adv. Energy Mater.* **2018**, *8*, 1800944.
[126] S. Y. Kim, D. Kundu, L. F. Nazar, *Adv. Energy Mater.* **2018**, *8*, 1701729.
[127] G. Santoro, J. M. Amarilla, P. Tartaj, M. B. Vázquez-Santos, *Mater. Today energy* **2018**, *10*, 23-27.
[128] M. V. Zakharkin, O. A. Drozhzhin, I. V. Tereshchenko, D. Chernyshov, A. M. Abakumov, E. V. Antipov, K. J. Stevenson, *ACS Appl. Energy Mater.* **2018**, *1*, 5842-5846.
[129] D. Saurel, M. Galceran, M. Reynaud, H. Anne, M. Casas-Cabanas, *Int. J. Energy Res.* **2018**, *42*, 3258-3265.
[130] Y. Qi, Z. Tong, J. Zhao, L. Ma, T. Wu, H. Liu, C. Yang, J. Lu, Y.-S. Hu, *Joule* **2018**, *2*, 2348-2363.
[131] V. M. Kovrugin, J.-N. Chotard, F. Fauth, A. Jamali, R. David, C. Masquelier, *J. Mater. Chem. A* **2017**, *5*, 14365-14376.
[132] M. Bianchini, P. Xiao, Y. Wang, G. Ceder, *Adv. Energy Mater.* **2017**, *7*, 1700514.
[133] R. Liu, G. Xu, Q. Li, S. Zheng, G. Zheng, Z. Gong, Y. Li, E. Kruskop, R. Fu, Z. Chen, K. Amine, Y. Yang, *ACS Appl. Mater. Interfaces* **2017**, *9*, 43632-43639.
[134] R. Essehli, H. Ben Yahia, K. Maher, M. T. Sougrati, A. Abouimrane, J. B. Park, Y. K. Sun, M. A. Al-Maadeed, I. Belharouak, *J. Power Sources* **2016**, *324*, 657-664.
[135] J. C. Pramudita, R. Aughterson, W. M. Dose, S. W. Donne, H. E. Brand, N. Sharma, *J. Mater. Res.* **2015**, *30*, 381-389.
[136] J. Wang, B. Qiu, X. He, T. Risthaus, H. Liu, M. C. Stan, S. Schulze, Y. Xia, Z. Liu, M. Winter, J. Li, *Chem. Mater.* **2015**, *27*, 4374-4379.
[137] P. Serras, V. Palomares, T. Rojo, H. E. Brand, N. Sharma, *J. Mater. Chem. A* **2014**, *2*, 7766-7779.
[138] M. Galceran, D. Saurel, B. Acebedo, V. V. Roddatis, E. Martin, T. Rojo, M. Casas-Cabanas, *Phys. Chem. Chem. Phys.* **2014**, *16*, 8837-8842.
[139] J. Gaubicher, F. Boucher, P. Moreau, M. Cuisinier, P. Soudan, E. Elkaim, D. Guyomard, *Electrochem. Commun.* **2014**, *38*, 104-106.
[140] X. Yu, H. Pan, W. Wan, C. Ma, J. Bai, Q. Meng, S. N. Ehrlich, Y.-S. Hu, X.-Q. Yang, *Nano letters* **2013**, *13*, 4721-4727.
[141] C. Wang, D. Du, M. Song, Y. Wang, F. Li, *Adv. Energy Mater.* **2019**, *9*, 1900022.
[142] J. Li, X. He, S. Ostendorp, L. Zhang, X. Hou, D. Zhou, B. Yan, D. M. Meira, Y. Yang, H. Jia, *Electrochim. Acta* **2020**, *342*, 135928.
[143] Y. Tang, W. Li, P. Feng, M. Zhou, K. Wang, Y. Wang, K. Zaghib, K. Jiang, *Adv. Funct. Mater.* **2020**, *30*, 1908754.
[144] B. Xie, L. Wang, J. Shu, X. Zhou, Z. Yu, H. Huo, Y. Ma, X. Cheng, G. Yin, P. Zuo, *ACS Appl. Mater. Interfaces* **2019**, *11*, 46705-46713.
[145] W. Tang, Y. Xie, F. Peng, Y. Yang, F. Feng, X. Z. Liao, Y. S. He, Z. F. Ma, Z. Chen, Y. Ren, *J. Electrochem. Soc.* **2018**, *165*, A3910-A3917.
[146] J. Sottmann, F. L. M. Bernal, K. V. Yusenko, M. Herrmann, H. Emerich, D. S. Wragg, S. Margadonna, *Electrochim. Acta* **2016**, *200*, 305-313.
[147] J. C. Pramudita, S. Schmid, T. Godfrey, T. Whittle, M. Alam, T. Hanley, H. E. Brand, N. Sharma, *Phys. Chem. Chem. Phys.* **2014**, *16*, 24178-24187.
[148] Z. Dai, U. Mani, H. T. Tan, Q. Yan, *Small Methods* **2017**, *1*, 1700098.
[149] C. Delmas, C. Fouassier, P. Hagenmuller, *Physica B+ c* **1980**, *99*, 81-85.
[150] M. Bianchini, J. Wang, R. J. Clément, B. Ouyang, P. Xiao, D. Kitchaev, T. Shi, Y. Zhang, Y. Wang, H. Kim, M. Zhang, J. Bai, F. Wang, W. Sun, G. Ceder, *Nat. Mater.* **2020**, *19*, 1088-1095.
[151] M. H. Han, E. Gonzalo, G. Singh, T. Rojo, *Energy Environ. Sci.* **2015**, *8*, 81-102.
[152] N. Yabuuchi, K. Kubota, M. Dahbi, S. Komaba, *Chem. Rev.* **2014**, *114*, 11636-11682.
[153] J. Kim, D.-H. Seo, H. Kim, I. Park, J.-K. Yoo, S.-K. Jung, Y.-U. Park, W. A. Goddard III, K. Kang, *Energy Environ. Sci.* **2015**, *8*, 540-545.

[154] S.-M. Oh, S.-T. Myung, J. Hassoun, B. Scrosati, Y.-K. Sun, *Electrochem. Commun.* **2012**, *22*, 149-152.
[155] Y. Zhu, Y. Xu, Y. Liu, C. Luo, C. Wang, *Nanoscale* **2013**, *5*, 780-787.
[156] H.-W. Lee, R. Y. Wang, M. Pasta, S. W. Lee, N. Liu, Y. Cui, *Nat. Commun.* **2014**, *5*, 1-6.
[157] A. Ponrouch, A. Goñi, M. R. Palacin, *Electrochem. Commun.* **2013**, *27*, 85-88.
[158] X. Dou, I. Hasa, D. Saurel, C. Vaalma, L. Wu, D. Buchholz, D. Bresser, S. Komaba, S. Passerini, *Mater. Today* **2019**, *23*, 87-104.
[159] D. Stevens, J. Dahn, *J. Electrochem. Soc.* **2001**, *148*, A803.
[160] D. Stevens, J. Dahn, *J. Electrochem. Soc.* **2000**, *147*, 4428.
[161] S. Alvin, D. Yoon, C. Chandra, H. S. Cahyadi, J.-H. Park, W. Chang, K. Y. Chung, J. Kim, *Carbon* **2019**, *145*, 67-81.
[162] Z. V. Bobyleva, O. A. Drozhzhin, K. A. Dosaev, A. Kamiyama, S. V. Ryazantsev, S. Komaba, E. V. Antipov, *Electrochim. Acta* **2020**, *354*, 136647.
[163] M. Anji Reddy, M. Helen, A. Groß, M. Fichtner, H. Euchner, *ACS Energy Lett.* **2018**, *3*, 2851-2857.
[164] M. Fukunishi, N. Yabuuchi, M. Dahbi, J.-Y. Son, Y. Cui, H. Oji, S. Komaba, *The J. Phys. Chem. C* **2016**, *120*, 15017-15026.
[165] L. Liang, Y. Xu, C. Wang, L. Wen, Y. Fang, Y. Mi, M. Zhou, H. Zhao, Y. Lei, *Energy Environ. Sci.* **2015**, *8*, 2954-2962.
[166] N. K. Karan, M. D. Slater, F. Dogan, D. Kim, C. S. Johnson, M. Balasubramanian, *J. Electrochem. Soc.* **2014**, *161*, A1107.
[167] D. Dixon, M. Ávila, H. Ehrenberg, A. Bhaskar, *ACS omega* **2019**, *4*, 9731-9738.
[168] M.-K. Kim, S.-H. Yu, A. Jin, J. Kim, I.-H. Ko, K.-S. Lee, J. Mun, Y.-E. Sung, *Chem. Commun.* **2016**, *52*, 11775-11778.
[169] C. Guhl, P. Kehne, Q. Ma, F. Tietz, L. Alff, P. Komissinskiy, W. Jaegermann, R. Hausbrand, *Rev. Sci. Instrum.* **2018**, *89*, 073104.
[170] M. Fehse, D. Bessas, A. Darwiche, A. Mahmoud, G. Rahamim, C. La Fontaine, R. P. Hermann, D. Zitoun, L. Monconduit, L. Stievano, *Batteries Supercaps* **2019**, *2*, 66-73.
[171] J. Sottmann, M. Herrmann, P. Vajeeston, A. Ruud, C. Drathen, H. Emerich, D. S. Wragg, H. Fjellvåg, *Chem. Mater.* **2017**, *29*, 2803-2810.
[172] T. Broux, T. Bamine, L. Simonelli, L. Stievano, F. o. Fauth, M. Ménétrier, D. Carlier, C. Masquelier, L. Croguennec, *The J. Phys. Chem. C* **2017**, *121*, 4103-4111.
[173] M. Pivko, I. Arcon, M. Bele, R. Dominko, M. Gaberscek, *J. Power Sources* **2012**, *216*, 145-151.
[174] W. Tang, X. Song, Y. Du, C. Peng, M. Lin, S. Xi, B. Tian, J. Zheng, Y. Wu, F. Pan, K. P. Loh, *J. Mater. Chem. A* **2016**, *4*, 4882-4892.
[175] Z. Jian, W. Han, X. Lu, H. Yang, Y. S. Hu, J. Zhou, Z. Zhou, J. Li, W. Chen, D. Chen, *Adv. Energy Mater.* **2013**, *3*, 156-160.
[176] D. Kim, E. Lee, M. Slater, W. Lu, S. Rood, C. S. Johnson, *Electrochem. Commun.* **2012**, *18*, 66-69.
[177] S.-M. Oh, S.-T. Myung, C. S. Yoon, J. Lu, J. Hassoun, B. Scrosati, K. Amine, Y.-K. Sun, *Nano letters* **2014**, *14*, 1620-1626.
[178] W. Chao, P. Fischer, T. Tyliszczak, S. Rekawa, E. Anderson, P. Naulleau, *Opt. Express* **2012**, *20*, 9777-9783.
[179] D. A. Shapiro, Y.-S. Yu, T. Tyliszczak, J. Cabana, R. Celestre, W. Chao, K. Kaznatcheev, A. D. Kilcoyne, F. Maia, S. Marchesini, *Nat. Photonics* **2014**, *8*, 765.
[180] R. Falcone, C. Jacobsen, J. Kirz, S. Marchesini, D. Shapiro, J. Spence, *Contemp. Phys.* **2011**, *52*, 293-318.
[181] J. Nelson Weker, M. F. Toney, *Adv. Funct. Mater.* **2015**, *25*, 1622-1637.
[182] M. Wolf, B. M. May, J. Cabana, *Chem. Mater.* **2017**, *29*, 3347-3362.
[183] D. P. Finegan, M. Scheel, J. B. Robinson, B. Tjaden, I. Hunt, T. J. Mason, J. Millichamp, M. Di Michiel, G. J. Offer, G. Hinds, D. J. L. Brett, P. R. Shearing, *Nat. Commun.* **2015**, *6*, 6924.

[184] S. D. M. Jacques, M. Di Michiel, S. A. J. Kimber, X. Yang, R. J. Cernik, A. M. Beale, S. J. L. Billinge, *Nat. Commun.* **2013**, *4*, 2536.
[185] G. Harding, J. Kosanetzky, U. Neitzel, *Med. Phys.* **1987**, *14*, 515-525.
[186] S. W. T. Price, K. Ignatyev, K. Geraki, M. Basham, J. Filik, N. T. Vo, P. T. Witte, A. M. Beale, J. F. W. Mosselmans, *Phys. Chem. Chem. Phys.* **2015**, *17*, 521-529.
[187] J. Wang, L. Wang, C. Eng, J. Wang, *Adv. Energy Mater.* **2017**, *7*, 1602706.
[188] Z. Yu, J. Wang, L. Wang, Y. Xie, S. Lou, Z. Jiang, Y. Ren, S. Lee, P. Zuo, H. Huo, G. Yin, Q. Pan, J. Wang, *ACS Energy Lett.* **2019**, *4*, 2007-2012.
[189] J. Sottmann, R. Homs-Regojo, D. S. Wragg, H. Fjellvåg, S. Margadonna, H. Emerich, *J. Appl. Crystallogr.* **2016**, *49*, 1972-1981.
[190] M. Herklotz, J. Weiss, E. Ahrens, M. Yavuz, L. Mereacre, N. Kiziltas-Yavuz, C. Drager, H. Ehrenberg, J. Eckert, F. Fauth, L. Giebeler, M. Knapp, *J. Appl. Crystallogr.* **2016**, *49*, 340-345.
[191] F. Rosciano, M. Holzapfel, H. Kaiser, W. Scheifele, P. Ruch, M. Hahn, R. Kotz, P. Novak, *J. Synchrotron Radiat.* **2007**, *14*, 487-491.
[192] C. Villevieille, T. Sasaki, P. Novak, *RSC Adv.* **2014**, *4*, 6782-6789.
[193] O. J. Borkiewicz, B. Shyam, K. M. Wiaderek, C. Kurtz, P. J. Chupas, K. W. Chapman, *J. Appl. Crystallogr.* **2012**, *45*, 1261-1269.
[194] J. B. Leriche, S. Hamelet, J. Shu, M. Morcrette, C. Masquelier, G. Ouvrard, M. Zerrouki, P. Soudan, S. Belin, E. Elkaïm, F. Baudelet, *J. Electrochem. Soc.* **2010**, *157*, A606-A610.
[195] C. Baehtz, T. Buhrmester, N. N. Bramnik, K. Nikolowski, H. Ehrenberg, *Solid State Ionics* **2005**, *176*, 1647-1652.
[196] K. Nikolowski, C. Baehtz, N. N. Bramnik, H. Ehrenberg, *J. Appl. Crystallogr.* **2005**, *38*, 851-853.
[197] O. J. Borkiewicz, K. M. Wiaderek, P. J. Chupas, K. W. Chapman, *The J. Phys. Chem. Letters* **2015**, *6*, 2081-2085.
[198] G. Ouvrard, M. Zerrouki, P. Soudan, B. Lestriez, C. Masquelier, M. Morcrette, S. Hamelet, S. Belin, A. M. Flank, F. Baudelet, *J. Power Sources* **2013**, *229*, 16-21.
[199] O. J. Borkiewicz, K. W. Chapman, P. J. Chupas, *PCCP* **2013**, *15*, 8466-8469.
[200] L. H. B. Nguyen, A. Iadecola, S. Belin, J. Olchowka, C. Masquelier, D. Carlier, L. Croguennec, *J. Phys. Chem. C* **2020**, *124*, 23511-23522.
[201] J. Leriche, S. Hamelet, J. Shu, M. Morcrette, C. Masquelier, G. Ouvrard, M. Zerrouki, P. Soudan, S. Belin, E. Elkaïm, *J. Electrochem. Soc.* **2010**, *157*, A606.
[202] J. Sottmann, V. Pralong, N. Barrier, C. Martin, *J. Appl. Crystallogr.* **2019**, *52*, 485-490.
[203] K. Rhodes, M. Kirkham, R. Meisner, C. M. Parish, N. Dudney, C. Daniel, *Rev. Sci. Instrum.* **2011**, *82*, 075107.
[204] P. Bleith, W. van Beek, H. Kaiser, P. Novák, C. Villevieille, *J. Phys. Chem. C* **2015**, *119*, 3466-3471.
[205] H. Liu, P. K. Allan, O. J. Borkiewicz, C. Kurtz, C. P. Grey, K. W. Chapman, P. J. Chupas, *J. Appl. Crystallogr.* **2016**, *49*, 1665-1673.
[206] J. Sottmann, M. Di Michiel, H. Fjellvåg, L. Malavasi, S. Margadonna, P. Vajeeston, G. B. M. Vaughan, D. S. Wragg, *Angew. Chem. Int. Ed.* **2017**, *56*, 11385-11389.
[207] J. Nelson, S. Misra, Y. Yang, A. Jackson, Y. Liu, H. Wang, H. Dai, J. C. Andrews, Y. Cui, M. F. Toney, *JACS* **2012**, *134*, 6337-6343.
[208] D. Verhoeven, *Appl. Opt.* **1993**, *32*, 3736-3754.
[209] P. Norby, *J. Am. Chem. Soc.* **1997**, *119*, 5215-5221.
[210] M. A. Newton, W. van Beek, *Chem. Soc. Rev.* **2010**, *39*, 4845-4863.
[211] J. Hanson, P. Norby, in *In-situ Characterization of Heterogeneous Catalysts*, Wiley Online Library, **2013**, pp. 121-146.
[212] N. Dobelin, **2009**.
[213] J. Rodriguez-Carvajal, in *Abstracts of the Satellite Meeting on Powder Diffraction of the XV Congress of the IUCr*, Toulouse, France, **1990**, p. 127.
[214] P. Rajiv, R. E. Dinnebier, M. Jansen, *Mater. Sci. Forum* **2010**, *651*, 97-104.
[215] B. Ravel, M. Newville, *J. Synchrotron Radiat.* **2005**, *12*, 537-541.

[216] N. K. Karan, M. D. Slater, F. Dogan, D. Kim, C. S. Johnson, M. Balasubramanian, *J. Electrochem. Soc.***2014**, *161*, A1107-A1115.
[217] G. W. Stinton, J. S. O. Evans, *J. Appl. Crystallogr.* **2007**, *40*, 87-95.
[218] A. Ruud, J. Sottmann, P. Vajeeston, H. Fjellvåg, *J. Mater. Chem. A* **2019**, *7*, 17906-17913.
[219] P. B. Samarasingha, J. Sottmann, S. Margadonna, H. Emerich, O. Nilsen, H. Fjellvåg, *Acta Mater.* **2016**, *116*, 290-297.
[220] J. Sottmann, R. Homs-Regojo, D. S. Wragg, H. Fjellvag, S. Margadonna, H. Emerich, *J. Appl. Crystallogr.* **2016**, *49*, 1972-1981.
[221] D. S. Wragg, M. G. O'Brien, M. Di Michiel, F. Lønstad-Bleken, *J. Appl. Crystallogr.* **2015**, *48*, 1719-1728.
[222] G. Agostini, C. Lamberti, L. Palin, M. Milanesio, N. Danilina, B. Xu, M. Janousch, J. A. Van Bokhoven, *J. Am. Chem. Soc.* **2010**, *132*, 667-678.
[223] A. Vamvakeros, A. A. Coelho, D. Matras, H. Dong, Y. Odarchenko, S. W. T. Price, K. T. Butler, O. Gutowski, A.-C. Dippel, M. Zimmermann, I. Martens, J. Drnec, A. M. Beale, S. D. M. Jacques, *J. Appl. Crystallogr.* **2020**, *53*, 1531-1541.
[224] A. Ruud, J. Sottmann, P. Vajeeston, H. Fjellvåg, *Phys. Chem. Chem. Phys.* **2018**, *20*, 29798-29803.
[225] L. Marbella, M. Evans, M. Groh, J. Nelson, K. Griffith, A. Morris, C. Grey, *J. Am. Chem. Soc.* **2018**, *140*, 7994-8004.
[226] J. Stratford, M. Mayo, P. Allan, O. Pecher, O. Borkiewicz, K. Wiaderek, K. Chapman, C. Pickard, A. Morris, C. Grey, *J. Am. Chem. Soc.* **2017**, *139*, 7273-7286.
[227] A. Jain, S. P. Ong, G. Hautier, W. Chen, W. D. Richards, S. Dacek, S. Cholia, D. Gunter, D. Skinner, G. Ceder, K. A. Persson, *APL Mater.* **2013**, *1*, 011002.
[228] G. Musumarra, G. Scarlata, S. Wold, *Gazz. Chim. Ital.* **1981**, *111*, 499-502.
[229] R. Caliandro, G. Di Profio, O. Nicolotti, *J. Pharm. Biomed. Anal.* **2013**, *78-79*, 269-279.
[230] A. Rizzuti, R. Caliandro, V. Gallo, P. Mastrorilli, G. Chita, M. Latronico, *Food Chem.* **2013**, *141*, 1908-1915.
[231] K. W. Chapman, S. H. Lapidus, P. J. Chupas, *J. Appl. Crystallogr.* **2015**, *48*, 1619-1626.
[232] A. M. C. Davies, T. Fearn, *Spectrosc. Eur.* **2004**, *16*, 20.
[233] R. Caliandro, V. Toson, L. Palin, E. Conterosito, M. Aceto, V. Gianotti, E. Boccaleri, E. Dooryhee, M. Milanesio, *Chem. – Eur. J.* **2019**, *25*, 11503-11511.
[234] P. Guccione, L. Palin, B. D. Belviso, M. Milanesio, R. Caliandro, *Phys. Chem. Chem. Phys.* **2018**, *20*, 19560-19571.
[235] E. Conterosito, L. Palin, R. Caliandro, W. van Beek, D. Chernyshov, M. Milanesio, *Acta Crystallogr., Sect. A* **2019**, *75*, 214-222.
[236] R. Caliandro, D. B. Belviso, *J. Appl. Crystallogr.* **2014**, *47*, 1087-1096.
[237] A. Darwiche, F. Murgia, M. Fehse, A. Mahmoud, A. Iadecola, S. Belin, C. La Fontaine, V. Briois, R. P. Hermann, B. Fraisse, R. Berthelot, M. T. Sougrati, L. Monconduit, L. Stievano, *Energy Storage Materials* **2019**, *21*, 1-13.
[238] L. H. Nguyen, A. Iadecola, S. Belin, J. Olchowka, C. Masquelier, D. Carlier, L. Croguennec, *The J. Phys. Chem. C* **2020**, *124*, 23511-23522.
[239] J. Felten, H. Hall, J. Jaumot, R. Tauler, A. de Juan, A. Gorzsás, *Nat. Protoc.* **2015**, *10*, 217-240.
[240] H. Motegi, Y. Tsuboi, A. Saga, T. Kagami, M. Inoue, H. Toki, O. Minowa, T. Noda, J. Kikuchi, *Sci. Rep.* **2015**, *5*, 15710.
[241] M. Garrido, F. X. Rius, M. S. Larrechi, *Anal. Bioanal. Chem.* **2008**, *390*, 2059-2066.
[242] P. Müller, I. Hermans, *Ind. Eng. Chem. Res.* **2017**, *56*, 1123-1136.
[243] A. Urakawa, T. Bürgi, A. Baiker, *Chem. Eng. Sci.* **2008**, *63*, 4902-4909.
[244] D. Chernyshov, V. Dyadkin, W. van Beek, A. Urakawa, *Acta Crystallogr., Sect. A: Found. Adv.* **2016**, *72*, 500-506.
[245] D. Chernyshov, I. Dovgaliuk, V. Dyadkin, W. van Beek, *Crystals* **2020**, *10*, 581.
[246] Z. Jiang, J. Li, Y. Yang, L. Mu, C. Wei, X. Yu, P. Pianetta, K. Zhao, P. Cloetens, F. Lin, Y. Liu, *Nat. Commun.* **2020**, *11*, 2310.

10.1002/batt.202000294

[247] V. Shapovalov, A. Guda, V. Butova, I. Shukaev, A. Soldatov, *Nanomaterials* **2021**, *11*, 156.
[248] J.-Q. Huang, X. Guo, J. Huang, H. Tan, X. Du, Y. Zhu, B. Zhang, *J. Power Sources* **2021**, *481*, 228916.
[249] B. T. Young, D. R. Heskett, C. C. Nguyen, M. Nie, J. C. Woicik, B. L. Lucht, *ACS Appl. Mater. Interfaces* **2015**, *7*, 20004-20011.
[250] L. A. Ma, A. J. Naylor, L. Nyholm, R. Younesi, *Angew. Chem. Int. Ed.* **2021**, *60*, 4855.